



Evolution of crystallographic preferred orientations of ice sheared to high strains by equal-channel angular pressing

Qinyu Wang^{1,2,3}, Sheng Fan³, Daniel H. Richards⁴, Rachel Worthington³, David J. Prior³, and Chao Qi^{1,2}

¹Key Laboratory of Earth and Planetary Physics, Institute of Geology and Geophysics, Chinese Academy of Sciences, Beijing, 100029, China

²College of Earth and Planetary Sciences, University of Chinese Academy of Sciences, Beijing, 101408, China

³Department of Geology, University of Otago, Dunedin, New Zealand

⁴Institute for Marine and Antarctic Studies, University of Tasmania, Hobart, 7005, Australia

Correspondence: Chao Qi (qichao@mail.iggcas.ac.cn)

Abstract. Plastic deformation of polycrystalline ice Ih induces crystallographic preferred orientations (CPOs), which give rise to anisotropy in the viscosity of ice, thereby exerting a strong influence on the flow of glaciers and ice sheets. The development of CPOs is governed by two pivotal mechanisms: recrystallization dominated by subgrain/lattice rotation and by strain-induced grain boundary migration (GBM). To examine the impact of strain on the transition of the dominant mechanism, synthetic ice (doped with ~ 1 vol.% graphite) was deformed using equal-channel angular pressing technique, enabling multiple passes to accumulate substantial shear strains. Nominal shear strains up to 6.2, equivalent to a nominal von Mises strain of $\epsilon' \approx 3.6$, were achieved in samples at a temperature of -5°C . Cryo-electron backscatter diffraction analysis reveals a primary cluster of crystal c axes perpendicular to the shear plane in all samples, accompanied by a secondary cluster of c axes at an oblique angle to the primary cluster antithetic to the shear direction. With increasing strain, the primary c -axis cluster strengthens, while the secondary cluster weakens. The angle between the clusters remains within the range of 45° to 60° . The c -axis clusters are elongated perpendicular to the shear direction, with this elongation intensifying as strain increases. Subsequent annealing of the highest-strain sample reveals the same CPO patterns as observed prior to annealing, albeit slightly weaker. A synthesis of various experimental data suggest that the CPO pattern, including the orientation of the secondary cluster, results from a balance of two competing mechanisms: lattice rotation due to dislocation slip, which fortifies the primary cluster while rotating and weakening the secondary one, and grain growth by strain-induced GBM, which reinforces both clusters while rotating the secondary cluster in the opposite direction. As strain increases, GBM contributes progressively less. This investigation supports the previous hypothesis that a single cluster of c axes could be generated in high-strain experiments, while further refining our comprehension of CPO development in ice.

1 Introduction

Ice, the solid phase of the most common compound in the universe, constitutes glaciers and ice sheets on Earth, polar ice caps on Mars, icy shells on icy satellites and a major part of many dwarf planets and asteroids in the solar system. The rheological behavior of ice Ih is critical to the ice-sheet dynamics on Earth (e.g., Gow and Williamson, 1976; Schoof and Hewitt, 2013;



Bons et al., 2016), viscous relaxation of topography on Mars and Ceres (e.g., Pathare et al., 2005; Bland et al., 2016), and convection and thermal evolution in the icy crust on Europa (e.g., Showman and Han, 2005; Barr and McKinnon, 2007).
25 During plastic deformation of ice, crystallographic preferred orientations (CPOs) are induced, which translate the kinematics of deformation into anisotropy in the microstructure, as ice is a highly anisotropic material. When deformed by dislocation glide, a single crystal of ice is several orders of magnitude weaker for slip on the basal plane, (0001), than on others (Duval et al., 1983). Once a CPO is formed in polycrystalline ice, it can lead to elastic and viscous anisotropies to ice, making shear parallel to the aligned basal planes easier and deformation in other orientations more difficult (Azuma, 1995). When the stress
30 field that drives ice flow changes, the rate of response will depend on the existing CPO and its subsequent evolution in the new stress configuration (Hudleston, 2015). Thus, the mechanical response of terrestrial and planetary ice bodies to climate, tidal and/or geological forcing depends, in part, on the evolution of their CPOs (e.g., Alley, 1992; Duval et al., 2010; Hudleston, 2015). Moreover, CPOs observed in natural ice samples (Jackson and Kamb, 1997; Jackson, 1999; Faria et al., 2014; Thomas et al., 2021) or derived from seismic data (e.g., Lutz et al., 2020, 2022) can provide valuable insights into the conditions and
35 history of ice deformation, in the same manner as CPOs for quartz (Schmid and Casey, 1986; Law, 2014) and olivine (Karato et al., 2008) that constrain deformation in the Earth's crust and mantle, respectively.

Many experimental studies focusing on the evolution of CPO in ice have found a transition of the crystallographic fabric, and attributed the transition to a change in the dominant mechanisms for CPO formation (e.g., Qi et al., 2017, 2019; Fan et al., 2020, 2021). As proposed by Alley (1992) and demonstrated by Qi et al. (2017), the dominant mechanism for CPO formation
40 changes from grain boundary migration (GBM) to lattice rotation and subgrain rotation (polygonization), with increasing stress, increasing strain or decreasing temperature (Qi et al., 2019; Fan et al., 2020). The two mechanisms are also referred to as migration recrystallization and rotation recrystallization (Poirier, 1985, pp. 179–185). Although uni-axial compression tests are the most used experimental techniques to study the microstructural evolution of ice during deformation, high-strain deformation in ice sheets and glaciers is dominantly simple shear (Cuffey and Paterson, 2010), and thus, understanding the CPO
45 evolution under shear is critical. Shear experiments on polycrystalline ice have found that the fabric transition from double-clustered to single-clustered [0001] axes (*c* axes) occurs with increasing strain (Kamb, 1972; Bouchez and Duval, 1982; Li et al., 2000; Wilson and Peternell, 2012; Qi et al., 2019). The highest shear strain ever achieved in laboratory, that is, 2.6, is reported by Qi et al. (2019) at -30°C , prior to which study, the shear experiments at similar temperatures have not achieved shear strains >0.12 (Wilson and Peternell, 2012). However, even at shear strains >2 , the [0001]-axis fabric has not evolved to
50 an absolute single cluster, instead the [0001] axes form a diffused cluster at $\gamma = 2.6$ at -30°C and a very weak secondary cluster at $\gamma = 2.2$ at -20°C (Qi et al., 2019). In contrast, natural ice samples that are known to have experienced high shear strains of >5 often exhibit a sharp, concentrated single cluster of [0001] axes (Hudleston, 1977; Jackson, 1999; Thomas et al., 2021). Meanwhile, numerical simulations incorporating dynamic recrystallization processes have found a single, primary cluster at smaller shear strains than experiments (Llorens et al., 2017; Piazzolo et al., 2019; Richards et al., 2021). This discrepancy leads
55 to an uncertainty on to whether the CPO in natural ice can be simply explained by the formation mechanisms proposed from experimental observations. Thus, new laboratory experiments to higher strains that are closer to those in naturally deformed ice are in need.



Equal-channel angular pressing (ECAP) is a technique for generating severe plastic deformation, resulting in highly strained microstructures with ultra-fine grain sizes and strong fabric. ECAP, also known as equal-channel angular extrusion, was initially developed in the 1980s by V.M. Segal and colleagues (Segal et al., 1981). Over several decades of development, ECAP has become the most widely used severe plastic deformation processing technique, employed in both academia and industry (Langdon, 2013; Segal, 2020). The general principles of ECAP are shown schematically in Figure 1. Processing by ECAP uses a die with two channels of equal cross-sectional area that intersect at an angle. The sample is machined to fit within the channel and then pressed through the die using a plunger under an applied pressure. To prevent sample fracturing within the channel, a back pressure is often applied from the outlet of the channel, confining the sample with a low pressure (e.g., Xia et al., 2005; Lapovok et al., 2008). The sample emerges from the die as shown on the right in Figure 1(c). Ideally, for steady and frictionless ECAP, the sample is sheared along the slip-line (line AO Figure 1(a)) in uniform, simple shear geometry. A round corner is usually used to accommodate the friction boundary conditions and eliminate the “dead zone” of no deformation. Notably, the cross-sectional dimensions of the sample remain unchanged after passing through the channel. This allows the sample to be pressed repeatedly through the channel, achieving a high shear strain. ECAP has been extensively used to investigate the microstructural evolution during severe plastic deformation of metals and alloys (e.g., Iwahashi et al., 1998; Zhao et al., 2004; Kawasaki et al., 2009), and thus can be an ideal tool to study the CPO evolution of ice sheared to high strains (Iliescu and Baker, 2008).

In this contribution, we adapt the ECAP method to polycrystalline ice. By conducting experiments at a warm temperature of -5°C , inhibiting grain growth with a small fraction of graphite particles (e.g., Song et al., 2005; Azuma et al., 2012; Saruya et al., 2019) and confining the sample with a small back pressure, we are able to press the samples through ECAP up to 6 passes, allowing us to shear ice to nominal shear strains of ~ 6.2 . The objective of this paper is to explore the effects of shear strain on the CPOs and microstructures of ice deformed in shear and to explore the implications for understanding the development of CPO in highly deformed natural ice.

2 Methods

2.1 Sample preparation

To prepare polycrystalline ice samples with a controlled initial microstructure, we adopted the flooding and freezing procedure developed by Durham et al. (1983) and Stern et al. (1997). The sample preparation procedure is the same as in Qi et al. (2019), except for that graphite powders with an average particle size of $2.6\ \mu\text{m}$ were added to the seed ice powders to inhibit ice grain growth during the deformation experiments. Samples fabricated this way has a graphite fraction of 1.8–3.6 wt.% (corresponding to 0.8–1.5 vol.%, more details please refer to Table 1). Previous experimental investigations have found that such small fractions of particles have no measurable effect on ice rheology, but result in smaller grain sizes than in particle-free ice (e.g., Jacka et al., 2003; Qi et al., 2018; Saruya et al., 2019).



2.2 ECAP die

90 A photo of the ECAP die is illustrated in Figure 1(a). The die consists of two symmetrical stainless-steel parts, each as half of the channel. Seven bolts alongside the channel fasten the two halves together, making a round and curved channel in the die. The diameter is 25 mm along the channel, the same as the diameter of our ice samples. The channel is “mirror finished” and coated with a layer of solid soap to minimize the friction for every experiment run. The channel is defined by two angles: the channel angle Φ represents the angle between the two parts of the channel (equal to 120° in Figure 1(a)), and the curvature angle Ψ represents the angle at the outer arc of curvature where the two parts of the channel intersect. The strain imposed in each pass of ECAP is dependent upon the angles Φ and Ψ . When a sample has fully passed through a corner, we refer to this as completing one pass of deformation, termed as “1 pass”. After the sample has fully passed through the corner n times, it is termed as “ N passes”. It can be shown from first principles that the equivalent strain after N passes, ε_N , is given by a relationship of the form (Iwahashi et al., 1996)

$$100 \quad \varepsilon_N = \frac{N}{\sqrt{3}} \left(2 \cot \left(\frac{\Phi}{2} + \frac{\Psi}{2} \right) + \Psi \operatorname{cosec} \left(\frac{\Phi}{2} + \frac{\Psi}{2} \right) \right). \quad (1)$$

For our design, $\Phi = 120^\circ$ and $\Psi \approx 60^\circ$, resulting an equivalent strain of ~ 0.6 (a shear strain of ~ 1.0) in the sample per pass.

2.3 Deformation experiments

The frame of the deformation apparatus is built with aluminum profiles. The ECAP die sits on a wide aluminum profile within a cooler box insulated with wool. Four Peltier coolers were attached to the flat surface of the ECAP die, with the cooling side stuck to the die and the heating side stuck to a water box. Both contact surfaces of coolers were covered with high-performance thermally conductive grease for efficient heat conduction. The water box acted as a heat sink and was linked to a water chiller, circulating 5°C water. Four thermistors (PT100) on the die monitored temperatures at locations illustrated in Figure 1(c) and (d). A proportional integral derivative (PID) controller regulated the Peltier coolers’ power based on the target temperature, set at -5°C for all experiments.

110 After cooling the die, a sample (at -30°C) was inserted in the channel, and a heat-insulating polymer plunger was inserted on top. An aluminum profile rested on the plunger and can slide vertically along two fixed aluminum pillars attached to the bottom profile. Once the temperature of the die stabilized (typically 20 min), indicating the sample temperature had equilibrated with the die, a load was applied to the sample using dead weights hung on the aluminum profile. The load was increased gradually, starting from 2.5 kg (weight of the plunger and profile) and reaching 22.5 kg in increments of 5 kg every 15 minutes. Further, 115 the load was increased from 22.5 kg to a maximum of 42.5 kg in 5 kg increments every 10 minutes. It is worth noting that as number of passes through the channel increases for single sample, the maximum load applied decreases slightly (more details please refer to Table 1 and Figure A1).

To provide a small back pressure to the sample, two double O-ring stainless-steel plugs were inserted into the channel from the outlet. The displacement of the sample was measured by a linear variable differential transformer (LVDT) as illustrated in 120 Figure 1. Temperature and displacement data were recorded every 10 seconds throughout each experiment. Since the plunger



cannot bend at the corner of the channel, when the tail of the sample reaches the corner of the channel, to push the whole sample through, a spare piece of ice is inserted (which won't be analyzed) to push the sample through the corner, completing a 1-pass experiment.

Upon passing through the channel, the sample's diameter remained unchanged, but the head and tail surfaces were no longer
125 perpendicular to the cylindrical axis, indicating shearing (see Figures 2 and 3). Subsequently, the head and tail surfaces were trimmed flat and parallel, restoring the sample's original shape except for a reduced length (Figure 2). The sample can be reinserted into the channel with the same orientation relative to the corner and deformed again. If the sample became shorter than 50 mm, an additional piece (which won't be analyzed) was added in the channel to achieve the required length (Figure 2). This process allows for multiple passes through the channel, accumulating high strains. After reaching the target number of
130 passes, the sample was wrapped in aluminum foil and stored in liquid nitrogen. Note that during an experiment, the head part of the sample was exposed to air, while the tail part was deformed in the corner, causing more sublimation in the head part. As a result, the head part was not ideal for microstructural analysis. Instead, the middle part near the tail was used for analysis in the next subsection.

To investigate the effect of annealing on pre-existing CPO, after ECAP deformation experiment, one sample was annealed
135 at -3.5°C for 24 days. The annealing experiment was done using a similar apparatus described in Fan et al. (2023).

2.4 Analysis of microstructure

Samples were prepared for cryogenic electron backscatter diffraction (EBSD) analysis in a scanning-electron microscope (SEM) at the University of Otago, following the procedure described in Prior et al. (2015). During preparation, a sample was either kept in a cryogenic dewar (at $\lesssim -190^{\circ}\text{C}$) or in an insulated transfer box (at $\lesssim -120^{\circ}\text{C}$). The sample was cut first in half
140 parallel to the profile plane and the cylinder axis, and then cut again parallel to the first cut to obtain a section of the profile plane (see Figure 3), using a band saw in a cold room maintained at -10°C . A small piece of the sample was also cut, melted and weighed to examine the exact graphite fraction. Sample mounting was done the same way as described in Prior et al. (2015).

To obtain a flat surface for EBSD analysis, the section surface was polished on sandpapers atop a flat metal plate at -80 to
145 -50°C , with a grit size of 400. To prevent graphite from covering the polished surface, the surface was not polished to high grit sizes that were used for pure water ice (Prior et al., 2015). The sample, mounted on the ingot, was transferred into the SEM and mounted on a cryostage, maintained $< -90^{\circ}\text{C}$, through a nitrogen-filled glove box (Prior et al., 2015). A pressure cycle was performed in the SEM chamber to remove frost on the sample surface (Prior et al., 2015).

Orientation and element data were collected simultaneously on a Zeiss Sigma VP field-emission-gun SEM equipped with
150 a Symmetry EBSD camera and a X-max energy dispersive spectroscopy (EDS) detector from Oxford Instruments. 2–5 Pa of nitrogen gas pressure were maintained in the chamber to minimize charging. Raw diffraction data were acquired and processed using the AZTEC software package. For each sample, an orientation map with a step size of $30\ \mu\text{m}$ was collected for the majority of the section, and several smaller orientation maps with a finer step size of $15\ \mu\text{m}$ were collected for selected regions



on this section. Subsequently, carbon element data were obtained from EDS in the same regions with a step size ranging from
155 3.2 to 6.7 μm .

Orientation data obtained from diffraction data with a step size of 30 μm were not processed for extrapolation of unindexed points. These sets of data were used for analyzing the CPO patterns. Orientation data with a step size of 15 μm were processed using the MTEX toolbox (Bachmann et al., 2011) in MATLAB. Since graphite, the secondary phase in the samples, cannot be reliably detected in EBSD, we used the results from EDS to locate the graphite. The data were used to define the pixels
160 that correspond to graphite. As illustrated in Figure 4(a), the brightness in the EDS map represents different graphite signal intensities (from 1 to 6), with higher brightness indicating a higher content. The pixel proportion occupied by the graphite signal is approximately 17.8%, significantly surpassing the actual 1 vol.% graphite content. A threshold of intensity ≥ 2 was then applied to the data, removing very weak signals that may result from noise (Figure 4(b)). This is because the activation volume for X rays is large. In an ice+graphite sample, X rays are sampled from a volume of ice several micrometers in diameter. Areas
165 with low carbon signals may represent a small number of graphite particles in a larger volume of ice. To match the dimensions of the EBSD data, the pixel size of EDS map was adjusted to match the step size of EBSD. Then these pixels were attributed to graphite phase in EBSD data. Combine the EBSD data from ice and graphite, a data set with two phases was obtained (Figure 4(e)). Then the orientation map was filled via interpolation. Note that this method cannot identify individual graphite particles, but only revealed graphite-rich regions. With this method, the processed data generally contain a higher graphite fraction, as
170 the spatial resolution of EDS is relatively low and cannot identify individual graphite particles with 1 micron sizes.

Ice grains were then reconstructed from the processed data using the MTEX algorithm (Bachmann et al., 2010) with a grain boundary threshold of 10° . Grain size was determined as the equivalent diameter of a circle with the area of each grain in cross section. Note that grain size determined this way represents the size of a 2-D cross section of a 3-D grain. In the analysis of the average grain size for a map, grains containing no more than 5 pixels or lying on the edge of the map were excluded.

175 Orientation distributions were generated from the complete set of orientation data obtained using a step size of 30 μm using the MTEX toolbox in MATLAB (Bachmann et al., 2010; Mainprice et al., 2015). To quantify the strength of the CPOs, both the J-index (Bunge, 1982) and the M-index (Skemer et al., 2005) were used. From uniformly distributed orientations to a single-crystal orientation, the J-index, based on a calculated orientation distribution function, increases from 1 to infinity, while the M-index, based on the distribution of random-pair misorientation axes, increases from 0 to 1.

180 Since the CPOs of sheared ice are often characterized by double clusters of *c* axes (e.g., Kamb, 1972; Bouchez and Duval, 1982; Jackson, 1999; Qi et al., 2019), an angle, φ , was used to quantify the relative orientation between the two clusters. We adopted the same method used previously in Qi et al. (2019). The normalized counts of data per orientation in the profile plane were plotted on a histogram. φ was defined as that between the two peaks on the histogram.

2.5 Simulations from SpecCAF model

185 This CPOs were compared to predictions from the SpecCAF model (Richards et al., 2021). The SpecCAF model cannot directly simulate microstructural change that can be achieved by other models, e.g., ELLE, (Jessell et al., 2001). Instead, SpecCAF simulates the evolution of CPO, which is achieved through modeled processes involving grain rotation, diffusion



that simulates rotational recrystallization, and an orientation-dependent source term that emulates migration recrystallization (Richards et al., 2021). Nevertheless, the results from the SpecCAF model agree well with the CPOs reported in deformation experiments performed in Craw et al. (2018) and Qi et al. (2019). Consequently, the model can be used as a proxy to compare the samples in this study to how the CPO of pure ice would evolve at very high strains.

The numerical model was the same as those reported in Richards et al. (2021), producing simulated pole figures and the angle, φ . φ , was compared to model predictions with a variety of $\beta = k\beta_0$ values, where β controls the magnitude of the effect of migration recrystallization on the modelled CPO, $0 \leq k < 1$, and β_0 represents the value found for natural ice at $T = -5^\circ\text{C}$. Different values of k were used to assess the relative contributions of GBM and lattice rotation to CPO.

3 Results

3.1 Starting material

The ice microstructure of the starting materials was similar in character to that described in (Qi et al., 2017). The microstructure of an undeformed sample is illustrated in Figure 5. The undeformed sample has a roughly homogeneous ice microstructure. Graphite particles form graphite clusters and graphite-rich regions approximately uniformly distributed between ice grains. The mean ice grain size is $150\ \mu\text{m}$, rather smaller than pure polycrystalline ice made in a similar method (e.g., Qi et al., 2017). The initial crystallographic orientation is approximately random with a M-index of 0.002 and a J-index of 1.08. There are very few intragranular distortions, as shown by very few subgrain boundaries within the grains.

3.2 Mechanical data

The plot of displacement and temperature versus time for 6 passes of sample ECAP_38 is illustrated in Figure 6, while plots for other samples are illustrated in Appendix Figure A1. The temperature, monitored at the corner of the channel, was stable throughout an experiment run. The temperature variation for the 1st to 5th pass is within 0.2°C , with an average temperature of approximately -5°C , but the 6th pass shows a larger perturbation and a slightly lower average temperature ($\sim 0.5^\circ\text{C}$), likely due to variations in laboratory temperature and humidity. After the progressive initial loading process, all experiment runs were conducted at a constant load. The displacement typically increased rapidly with time in the first few hours due to compaction and bending of the sample's head (refer to Figure 1 for the "head" of the sample). Then displacement increased roughly linearly with time as the sample deforms at a nearly steady state, and increased rapidly again in the last few hours caused by the loss of back pressure, where the plug is pushed out of the channel by the sample. The 1st pass is generally much slower than the subsequent runs, despite having a higher load.

Load and displacement data from ECAP experiments have not been extensively used for in-depth analysis of mechanical properties (see Valiev and Langdon, 2006, for a review). This limitation is primarily due to the fact that only the portion at the corner of the channel undergoes deformation during pressing. Finite element analyses reveal complicated stress and strain fields around the corner (e.g., Kvackaj et al., 2007; Wei et al., 2009). As the sample passes through the corner, the material



experiences a significant change in stress, transitioning from none to a high value and then back to none. Consequently, such
220 data are not well-suited for rigorous investigations of mechanical behaviors.

However, as ECAP is a relatively new technique for ice, the deformation pathway the sample experiences during pressing
is described here. For each pass, the deformation starts at the head of the sample while the rest of the sample is annealed
at $\lesssim -5^{\circ}\text{C}$. Over time, the stress in the head part gradually increases to a maximum, then decreases to zero, resulting in a
nominal equivalent strain of ~ 0.6 in the deformed part. After this, the deformed head simply slides through the outlet tube,
225 experiencing no deformation and annealing at $\lesssim -5^{\circ}\text{C}$. The ice behind the head passes through the corner after the head and
is also strained. The tail is the last part of the sample to pass through the corner and be strained. A point in the sample only
experiences shear stress when passing through the corner. During the rest of the time, the sample anneals. Figure 6(c) shows
the straining-annealing sequence for the 6-pass sample. In each pass, the head undergoes strain at a rate of 1.5×10^{-6} (1st pass)
to 3×10^{-6} (6th pass) s^{-1} for $\sim 30\%$ time (~ 100 h for 1st pass and ~ 50 h for 6th pass) and is then annealed for $\sim 70\%$ time
230 (~ 270 h for 1st pass and ~ 120 h for 6th pass). Ice in the middle of the sample undergoes annealing for $\sim 35\%$ time (~ 130 h for
1st pass and ~ 60 h for 6th pass) before straining and $\sim 35\%$ time (~ 130 h for 1st pass and ~ 60 h for 6th pass) after straining.
The tail anneals for $\sim 70\%$ time (~ 270 h for 1st pass and ~ 120 h for 6th pass) before straining. We note that the samples
were deformed differently from those reported in previous studies, in which the whole sample deformed simultaneously (e.g.,
Kamb, 1972; Qi et al., 2019), rather than having a deformation front passing through the sample. Thus, we will refer to our
235 strain as the nominal strain, denoted by ε' .

3.3 Crystallographic preferred orientations

In this subsection, CPOs in all samples deformed to different strains (different numbers of ECAP passes) are described, as
illustrated in Figure 7. The CPOs of all samples feature two clusters of c axes. The primary cluster consistently aligns per-
pendicular to the imposed shear plane at all strains, while the secondary cluster is situated in the profile plane antithetic to the
240 shear direction. The CPO strength, as revealed by J- and M-indexes, generally increases with increasing strain, as illustrated
in Figure 8. In all samples, the elongation of c -axes clusters is observed sub-perpendicular to the shear direction. The primary
cluster becomes more elongated with increasing strain, while the secondary cluster becomes less elongated, as illustrated in
Figure 9.

The angle between clusters varies between 45° and 60° for all samples, being roughly constant with increasing strain. Except
245 for ECAP_33_1P ($\varepsilon'_1 \approx 0.6$), the sample with the lowest strain, the strengths of the secondary clusters in all samples are weaker
(indicated by a lower value of multiples of uniform density, MUD) compared to the primary clusters. A comparison between the
strength of the two clusters suggests that the secondary cluster generally weakens with increasing strain. A more quantitative
comparison is given in Figure 8(c). The logarithm of the ratio of data-point number in the primary and the secondary clusters
increases with increasing strain.

250 In all samples, the CPOs are characterized by prominent girdles of $[11\bar{2}0]$ axes (a axes) and $[10\bar{1}0]$ axes (poles to m planes)
within the shear plane, along with weaker girdles of $[11\bar{2}0]$ and $[10\bar{1}0]$ axes perpendicular to the secondary c -axis clusters. In
the two samples with $\varepsilon' \geq 3.0$, a axes strongly concentrate parallel to the shear direction; while in the sample with lower strains,



the distribution of a axes is more uniform in the girdles with some maxima parallel to the vorticity axis. The distributions of the poles to m plane are similar to the distributions of a axes in all samples.

255 3.4 Microstructure

The microstructures, grain-size distributions and shape distributions for all samples are presented in Figure 10. Note that the analyses of grain size are based on larger areas (4–6 times) than those presented in the maps. The presence of graphite particles in the samples induces many difficulties in the analyses of microstructure. To prevent graphite from covering the sample surface, the surface cannot be polished down to grit sizes finer than 400. Moreover, graphite conducts heat when scanned by
260 the electron beam, which accelerates sublimation of ice next the graphite and results in areas of unindexed points larger than the graphite particle. Although we processed the microstructure incorporating the EDS analysis, the grain boundaries reconstructed from orientation data are affected by the identified graphite phase. All samples are characterized by lobate grain boundaries and irregular grain shapes. Many grains are elongated, especially in the high-strain samples. Subgrain boundaries are observed in all samples, and are more in the samples with higher strains.

265 In all samples, the distributions of grain size are skewed, with a peak at finer grain sizes and a long tail extending to coarser grain sizes. In samples deformed to 1 to 3 passes ($\epsilon' \leq 1.8$), grain sizes vary greatly, with many grains larger than 500 μm and many smaller than 100 μm . In samples deformed to 4–6 passes ($\epsilon' \geq 2.4$), the deviation in grain size is smaller, the grain-size distribution is better fit by a log-normal distribution (oranges in Figure 10(b)), and the mean grain size is similar to the starting grain size. In all samples, grains are elongated after deformation and form clear shape preferred orientations (SPOs).
270 The distribution of aspect ratios varied very little in samples deformed to 2 to 6 passes. All samples have a SPO with a long axis of $\sim 10^\circ$ to the shear direction, except for the 1-pass sample, where the angle is 32° .

4 Discussion

CPOs of all deformed samples are characterized by two c -axis clusters. The angle between the two clusters stabilizes between 45° and 60° as strain increases. Before comparing our results with previous studies, we need to discuss the influences of ex-
275 perimental settings introduced in this study. ECAP deformation utilized in our study differs from simultaneous deformation applied to the entire sample in compression, shear and torsion experiments (e.g., Kamb, 1972; Durham et al., 1992; Li et al., 2000; Journaux et al., 2019; Qi et al., 2019). In our experiments, apart from the single-pass sample (ECAP_33_1p), which underwent a single deformation and annealing, the multi-pass sample experienced cyclic deformation and annealing. Additionally, to slow down grain growth, we introduced ~ 1 vol.% graphite particles into the sample. The potential influence of a
280 second phase on the evolution of CPO must be taken into account. We will focus on the influences of annealing and graphite in the following two subsections, and then perform a careful comparison with CPOs observed in laboratory experiments, field samples and models.



4.1 Influence of annealing

As described in Section 3.2, during an ECAP experiment, a sample was annealed before and/or after passing through the corner.
285 Here, we look at the influence of annealing on CPO. The sample annealed at -3.5°C for 24 days has the same CPO patterns as the original sample ECAP_38_6p before annealing, but the strength of the secondary cluster increases, as illustrated in Figure 7. The CPO also slightly weakens after annealing, as illustrated in Figure 8. This observation is in good agreement with previous studies. Wilson (1982) performed annealing experiments at -1°C on samples previously deformed at -10 and -1°C . He reported that the annealing did not significantly change the CPO patterns in the -1°C samples, but modified the patterns
290 in the -10°C samples. Hidas et al. (2017) carried out annealing experiments at -5 and -2°C up to a maximum of 78 h on samples deformed at -7°C . The authors found that grain growth proceeds at the expense of domains with high intragranular misorientations, consuming first the most misorientated parts of primary grains. Journaux et al. (2019) carried out an annealing experiment at -7°C for 72 h on a sample sheared in torsion at -7°C . These authors reported a much larger grain size in the annealed sample, suggesting strong GBM; however, they found that the pre-existing CPO pattern was not modified by the
295 annealing. Fan et al. (2023) performed annealing experiments at 0°C on natural samples from the Priestley Glacier, Antarctica, and reported that CPO was modified only when abnormal grain growth occurred after at least 72 hours.

Based on the above discussion, we suggest that annealing will not alter the patterns of CPO obtained after deformation, but can slightly weaken the strength of CPO. Here, we explore the influence of cyclic annealing on the evolution of CPO during subsequent ECAP passes. During annealing, dislocation density and strain energy are reduced by recrystallization
300 (Poirier, 1985). At the same nominal strain, a sample that just experienced annealing may have a lower dislocation density compared to a sample continuously deformed without annealing. Consequently, in subsequent deformation, additional strain should be required to compensate for the reduced dislocation density and strain energy resulted from annealing, reaching the threshold to initiate dynamic recrystallization (Bacca et al., 2015). Thus, given the same nominal strain, the effect of strain on microstructure in our ice samples could be weaker than that in ice samples deformed continuously. In other words, the nominal
305 strains calculated from Eq. 1 in our experiments could be an overestimation for CPO evolution, which could explain the lower CPO strength compared with the samples in Qi et al. (2019).

4.2 Influence of second phase

Here we investigate the impact of doping ~ 1 vol.% graphite on the evolution of CPO. Cyprych et al. (2016) and Wilson et al. (2019) conducted axial compression experiments on pure D_2O ice and D_2O ice doped with 20 or 40 vol.% graphite (< 150 or
310 $150\text{-}355$ μm in diameter), or 20 or 40 vol.% calcite (< 150 or $150\text{-}355$ μm in diameter) at temperatures 10°C below the melting point (actual at -7°C) and ambient pressures. All two-phase samples exhibited ice CPO patterns that were remarkably similar to those of single-phase samples, albeit with a weaker CPO intensity compared to single-phase samples. Cyprych et al. (2016) and Wilson et al. (2019) suggested that the mechanisms influencing CPO development in two-phase samples and ice-only samples are consistent, involving GBM and nucleation, where GBM may be hindered by the second phase. Song et al. (2005)
315 conducted axial compression experiments on pure water ice and ice doped with 1 wt.% (~ 0.43 vol.%) soil particles (sieved to



50±10 μm) at −10°C. They found a more random orientation of *c* axes, that is, weaker fabric, after a strain of ~0.1 in ice with particles than in particle-free ice. In our samples, the fraction of the second phase is much lower than the samples of Cyprych et al. (2016) and Wilson et al. (2019), and the strain is much larger than the samples of Song et al. (2005). Extrapolated from their results, we think the graphite doped in our sample may reduce the intensity of CPO, but cannot alter the CPO patterns.

320 Due to rapid grain growth, we could not perform an ECAP experiment on particle-free ice without fracturing it. So a small fraction of graphite was added to inhibit grain growth. Based on the discussion above, we think the CPOs in our samples are comparable with the CPOs in previous studies.

Based on the discussions in Sections 4.1 and 4.2, we suggest that the patterns of CPO observed in our experiments can be compared with those reported in previous studies. The CPO evolution with increasing strain could be slower than those in

325 previous studies, as the nominal strains of our samples are possibly overestimated. Consequently, in the following discussions, we focus on CPO patterns.

4.3 The elongated *c*-axis clusters

In our experiments, both primary and secondary clusters are elongated in the direction sub-perpendicular to the shear direction. These observations are consistent with studies on ice samples deformed primarily by simple shear in laboratory settings, for

330 which CPOs with substantial measured grain have been reported (Kamb, 1972; Bouchez and Duval, 1982; Li et al., 2000; Qi et al., 2019; Journaux et al., 2019). Li et al. (2000) attributed elongated clusters to extensional deformation in the shear plane, perpendicular to the shear direction, induced by the flattening of the sample during shear deformation. However, elongation was also observed in samples sheared by torsion, in which no axial load was applied and the deformation kinematics were ensured to be simple shear (Bouchez and Duval, 1982; Journaux et al., 2019). Meanwhile, natural ice samples from shear

335 zones provide diverse results. The CPOs reported in Hudleston (1977) for a glacial shear zone are all characterized by round *c*-axis clusters. The CPOs reported in Jackson (1999) and Jackson and Kamb (1997) for an ice stream marginal shear zone, however, have elongated *c*-axis clusters perpendicular to the shear direction. Recently, studies with modern EBSD technique provide much more data for CPOs in natural ice samples. Monz et al. (2021) found an elongated primary *c*-axis cluster in a shear-dominated region of a valley glacier; while Thomas et al. (2021) found a roughly round primary *c*-axis cluster in the

340 shear margin of a glacier. Furthermore, the elongated cluster is also observed in numerical simple-shear simulations by Llorens et al. (2016, 2017) and Richards et al. (2021), in which no flattening strain is allowed. Richards et al. (2021) found that *c*-axis clusters were elongated primarily due to lattice rotation. Thus, we hypothesize that the elongation of clusters results from rotation recrystallization. At larger strains, most grains have their *c* axes aligned sub-normal to the shear plane. When rotation recrystallization occurs, the orientations of the nuclei are different from the host grains, resulting in a dispersion of orientations

345 (see Figure 12(c)). Lattice rotation tends to rotate the *c* axes of the nuclei back to the normal to the shear plane. The rotation process is easier when the rotation axis is in the same orientation as the vorticity axis of deformation, that is, the rotation is in the shear direction normal to the shear plane (Rathmann et al., 2021). Comparatively, the rotation process is slower when the rotation is normal to the shear direction. This process results in *c* axes spreading normal to the shear direction. The round



clusters observed in glaciers could be explained by that the stress and temperature conditions favor migration recrystallization
350 over rotation recrystallization. We hope to further investigate the cause of the elongated clusters in the future.

4.4 The evolution of the *c*-axis clusters: comparison with experiments

Figure 11 illustrates the evolution of the angle between clusters, φ , as strain increases, comparing with data from prior exper-
imental studies, numerical models, and naturally deformed ice. This figure was plotted in the same manner as Figure 8 in Qi
et al. (2019), focusing on a temperature of $-5\pm 4^\circ\text{C}$. The values of φ are scattered between 43 and 81° for all experimental
355 samples with double *c*-axis clusters.

At warm temperatures ($-5\pm 4^\circ\text{C}$), Li et al. (2000) remains the only study that reported a single *c*-axis cluster at a shear
strain < 2.5 . However, as pointed out by Qi et al. (2019), Wilson and Peternell (2012) present more complex patterns of CPOs,
which are characterized by double-cluster patterns at a shear strain of ~ 1 at -2°C , despite conducting their experiments using
the same apparatus and kinematic constraints as Li et al. (2000). The two recent studies both reported double-cluster CPOs at
360 warm temperatures (Qi et al., 2019; Journaux et al., 2019). Qi et al. (2019) hypothesized that the key element in generating a
single cluster is high shear strain. In this study, the CPOs were characterized by double *c*-axis clusters below a nominal shear
strain of ~ 6.2 , but the secondary cluster became very weak at this maximum strain. It is worth noting that under the same
strain, the strength of the CPO in the sample deformed by ECAP is weaker than that in samples deformed continuously. This
result supports the earlier hypothesis that the contribution of GBM to CPO formation decreases with increasing strain.

365 The evolution of φ with strain is quite interesting. Based on the data in literature, one could tentatively suggest that φ
decreases with increasing strain (Qi et al., 2019). However, considering the results of this study, φ decreases to $\sim 50^\circ$ and
remains roughly constant until the secondary cluster weakens to almost invisible. This observation suggests that φ may not
necessarily change, instead the secondary cluster remains its orientation, and weakens with increasing strain. The model of
CPO development in (Qi et al., 2019) needs to be refined.

370 4.5 The evolution of the *c*-axis clusters: comparison with natural samples

In Qi et al. (2019), natural CPOs from a glacial shear zone reported by Hudleston (1977) were compared with the laboratory
CPOs in simple shear. The key agreements between natural and laboratory CPOs were that (1) the primary cluster maintains
a sub-perpendicular orientation to the shear plane at all shear strains; (2) the angle between two clusters diminishes as strain
increases; and (3) CPOs feature a solitary *c*-axis cluster at high strains. Here, we review these with new results from natural
375 (Monz et al., 2021; Thomas et al., 2021) and laboratory samples.

Monz et al. (2021) used a composite section method to obtain a representative, bulk CPO on a coarse-grained glacial ice sam-
ple from Storglaciären, Sweden. The results yielded a pronounced *c*-axis cluster sub-perpendicular to the shear plane. Thomas
et al. (2021) analyzed an ice core from the floating lateral shear margin of Priestley Glacier, Antarctica. They reported that
most samples have a single cluster sub-perpendicular to shear, with some samples having a secondary cluster. The agreements
380 in CPOs between natural and laboratory samples hold true for the orientation of the primary cluster and for the requirement
of a single cluster. In these natural samples (Hudleston, 1977; Monz et al., 2021; Thomas et al., 2021), the smallest value of



φ in samples with double clusters is 35° from the core at a depth of 2.4 m (Thomas et al., 2021). Due to its shallow depth, the microstructure of this sample was not developed completely due to plastic deformation, but may be affected by annealing and other processes. Besides this sample, the next smallest φ is 40° in a low strain sample from the shear zone (Hudleston, 1977). The absence of low angles ($<40^\circ$) between clusters in natural samples is in good agreement with laboratory data, and is possibly due to that the secondary cluster weakens with increasing strain, rather than moving towards the primary cluster. Thus, both natural observations and laboratory experiments suggest that the secondary cluster remains in its orientation and weakens until disappears with increasing strain.

4.6 The evolution of the c -axis clusters: comparison with numerical models

The evolution of the c -axis clusters was compared between CPOs from experiments and a FFT model (Llorens et al., 2017) in Qi et al. (2019). The numerical models fit some experimental observations but clearly need more work. The SpecCAF model, incorporating recrystallization, lattice rotation and grain rotation processes, yielded excellent quantitative agreement in the CPOs from experimental observations and numerical models (Richards et al., 2021). Applying this model to simple shear yields roughly constant values of φ with increasing strain at shear strains > 1 , when the effect of GBM is similar to or smaller than the value estimated for natural ice ($\varphi \approx 74^\circ, 71^\circ, 65^\circ$ and 60° for $\beta = 1, 0.8, 0.6$ and $0.5\beta_0$, respectively; Richards et al. (see 2021)). This result is in qualitative agreement with the experiments that the secondary cluster remains its orientation and weakens with increasing strain. When the effect of GBM is reduced to much weaker than natural ice ($\beta = 0.2\beta_0$), φ decreases to $<40^\circ$ with increasing strain and the fabric becomes a single c -axis cluster at a shear strain < 1 (the dark blue curve in Figure 11). This model suggests that lattice/subgrain rotation tends to move the secondary cluster towards the primary cluster, while GBM competes with rotation. The resulted angle between clusters is balanced by the two processes.

4.7 A refined model of CPO development in simple shear

Our earlier contribution (Qi et al., 2019) proposed that the CPO development of ice with increasing strain during simple shear was due to a transition in the dominant recrystallization process from lattice/subgrain rotation and GBM. Here we refine this model based on new experimental data, as illustrated in Figure 12.

GBM is usually driven by the difference in dislocation density of grains on both sides of the grain boundary, causing the grain boundary to migrate from the low-density side to the high-density side, thereby consuming grains with high density of dislocations (Urai et al., 1986). Grains with low resolved shear stresses, or Schmid factors, on the basal plane (also referred to as poorly oriented for easy basal slip), are have to deform through slip on non-basal slip systems. For ice, we hypothesize that these non-basal-slip dislocations are more difficult to glide, and there will be more than one interacting slip system. Therefore, grains with basal planes poorly oriented for easy (basal) slip tend to exhibit higher internal distortion (Vaughan et al., 2017). Grains with higher-Schmid factors on the basal plane tend to grow by consuming grains with lower-Schmid factors ((Figure 12(c))). In simple shear, basal planes parallel to the shear plane and normal to the shear direction are the two orientations with high Schmid factors. Thus, GBM generates two c -axis clusters, perpendicular to the shear plane (primary) and parallel to the shear direction (secondary).



415 Lattice rotation with basal glide produces a *c*-axis cluster perpendicular to the shear plane (primary). With increasing strain, this cluster strengthens rapidly, while *c* axes in other orientations are rotated towards this cluster. Subgrain rotation can trigger a nucleation process, leading to the generation of new small grains, which is commonly referred to as subgrain rotational recrystallization (Guillope and Poirier, 1979; Urai et al., 1986; Bestmann and Prior, 2003). Orientations of crystallographic axes in the recrystallized grains generally are randomly diffused equivalents of the stronger CPOs in the host grains (Jiang et al., 2000; Bestmann and Prior, 2003; Craw et al., 2018). We also hypothesize that in simple shear the dispersed orientations are easier to rotate back if the rotation axis is normal to the shear direction in the shear plane, and thus leading to a preferential dispersal of the *c* axes. Qi et al. (2019) also suggested the elongation of clusters may also relate to GBS-aided rotation around the vorticity axis synthetic to the shear direction. That hypothesis has not been tested yet.

Figure 12(d) is a refinement based on the schematic diagram proposed by Qi et al. (2019) illustrating the development of CPO patterns with shear strain, incorporating our experimental data. Due to the combined effect of lattice rotation and GBM, the initial CPO patterns feature two *c*-axis clusters normal to the shear plane and parallel to the shear direction. With increasing strain, the secondary cluster is weakened and rotated towards the primary cluster due to lattice rotation. During the deformation process, GBM will continue to promote the growth of grains with the *c* axes normal to the shear plane and parallel to the shear direction. Subgrain rotation recrystallization plays a critical role in forming the CPO by supplying providing grains with dispersed orientation, thereby providing grains for GBM. The orientation of secondary cluster is a result of the competition between lattice rotation and GBM. In the earlier model, the secondary cluster was thought to move towards the primary cluster continuously with increasing strain. A single cluster can thus develop as the secondary cluster merges into the primary cluster. In our refined model, given a steady-state deformation, the secondary cluster will be stationary with increasing strain, once a “balance” between lattice rotation and GBM is reached. With increasing strain, instead of moving, the secondary cluster progressively weakens, leading to the predominance of the primary. Such that there are fewer grains in low-Schmid-factor orientations, which will reduce the number of grains with high dislocation density, effectively reducing the driving force for GBM. Thus, with increasing strain, the contribution from GBM reduces, and the CPO will eventually become a single *c*-axis cluster fabric.

5 Conclusions

- 440 • Utilizing the ECAP technique, we achieved a nominal equivalent strain of ~ 3.6 (a nominal shear strain of ~ 6.2) in polycrystalline ice doped with ~ 1 vol.% graphite deformed at -5°C in roughly simple shear.
 - The cyclic annealing introduced by ECAP deformation, along with the presence of a small amount of graphite, may reduce the strength of the CPO, but will not alter the patterns of the CPO.
 - All samples develop a primary *c*-axis cluster perpendicular to the shear plane and a secondary *c*-axis cluster in the profile plane antithetic to the imposed shear direction. The orientation of the primary cluster does not change as a function of strain. The secondary cluster roughly remains its orientation but weakens as strain increases.



- Annealing of the 6-pass sample at -3.5°C for 24 days revealed the same CPO patterns as before annealing. The strength of this CPO became slightly weaker and the secondary cluster became slightly stronger after annealing.
- A combination of our data and published literature data, and comparisons with numerical models reveal the key processes that control the evolution of CPOs in ice during shear. The CPO patterns results from a balance of two competing mechanisms: lattice rotation due to dislocation slip, strengthening the primary cluster and rotating and weakening the secondary one, and growth of grains by strain-induced GBM, strengthening both clusters and rotating the secondary cluster back. GBM contributes less as shear strain increases.

Data availability. Data are available on an online data repository: Data of “Evolution of crystallographic preferred orientations of ice sheared to high strains by equal-channel angular pressing”. figshare. Dataset. <https://doi.org/10.6084/m9.figshare.23807400>

Author contributions. CQ and DJP designed the research. CQ designed the deformation equipment. QW performed experiments. QW, SF and RW performed analyses. DHR performed simulations. All authors participated in the interpretation of results. QW and CQ wrote the first draft, and all authors edited the manuscript.

Competing interests. The authors declare that they have no conflict of interest.

460

Acknowledgements. We thank to Prof. Jianhua Rao for his help with designing the ECAP die. This work was supported by a NSFC grant 41972232 (to CQ), the Key Research Program of the Institute of Geology and Geophysics, CAS, IGGCAS-201905 (to CQ), and Marsden Fund of the Royal Society of New Zealand UOO052 (to DJP).

Appendix A: Supplementary Figures

- Figure A1.



References

- Alley, R.B., 1992. Flow-law hypotheses for ice-sheet modeling. *Journal of Glaciology* 38, 245–256.
- Azuma, N., 1995. A flow law for anisotropic polycrystalline ice under uniaxial compressive deformation. *Cold regions science and technology* 23, 137–147.
- 470 Azuma, N., Miyakoshi, T., Yokoyama, S., Takata, M., 2012. Impeding effect of air bubbles on normal grain growth of ice. *Journal of Structural Geology* 42, 184–193.
- Bacca, M., Hayhurst, D.R., McMeeking, R.M., 2015. Continuous dynamic recrystallization during severe plastic deformation. *Mechanics of materials* 90, 148–156.
- Bachmann, F., Hielscher, R., Schaeben, H., 2010. Texture analysis with MTEX—free and open source software toolbox, in: *Solid State*
475 *Phenomena*, Trans Tech Publ. pp. 63–68.
- Bachmann, F., Hielscher, R., Schaeben, H., 2011. Grain detection from 2d and 3d EBSD data—specification of the MTEX algorithm. *Ultramicroscopy* 111, 1720–1733.
- Barr, A.C., McKinnon, W.B., 2007. Convection in ice I shells and mantles with self-consistent grain size. *Journal of Geophysical Research: Planets* 112.
- 480 Bestmann, M., Prior, D.J., 2003. Intragranular dynamic recrystallization in naturally deformed calcite marble: diffusion accommodated grain boundary sliding as a result of subgrain rotation recrystallization. *Journal of Structural Geology* 25, 1597–1613.
- Bland, M.T., Raymond, C.A., Schenk, P.M., Fu, R.R., Kneissl, T., Pasckert, J.H., Hiesinger, H., Preusker, F., Park, R.S., Marchi, S., et al., 2016. Composition and structure of the shallow subsurface of Ceres revealed by crater morphology. *Nature Geoscience* 9, 538–542.
- Bons, P.D., Jansen, D., Mundel, F., Bauer, C.C., Binder, T., Eisen, O., Jessell, M.W., Llorens, M.G., Steinbach, F., Steinhage, D., et al., 2016.
485 *Converging flow and anisotropy cause large-scale folding in Greenland’s ice sheet. Nature communications* 7.
- Bouchez, J.L., Duval, P., 1982. The fabric of polycrystalline ice deformed in simple shear: experiments in torsion, natural deformation and geometrical interpretation. *Texture, Stress, and Microstructure* 5, 171–190.
- Bunge, H.J., 1982. *Texture analysis in materials science: mathematical methods*. Butterworths London.
- Craw, L., Qi, C., Prior, D.J., Goldsby, D.L., Kim, D., 2018. Mechanics and microstructure of deformed natural anisotropic ice. *Journal of*
490 *Structural Geology* 115, 152–166.
- Cuffey, K.M., Paterson, W.S.B., 2010. *The physics of glaciers*. Academic Press.
- Cyprych, D., Piazzolo, S., Wilson, C.J., Luzin, V., Prior, D.J., 2016. Rheology, microstructure and crystallographic preferred orientation of matrix containing a dispersed second phase: Insight from experimentally deformed ice. *Earth and Planetary Science Letters* 449, 272–281.
- Durham, W.B., Heard, H.C., Kirby, S.H., 1983. Experimental deformation of polycrystalline H₂O ice at high pressure and low temperature: Preliminary results. *Journal of Geophysical Research: Solid Earth* 88, B377–B392. doi:<https://doi.org/10.1029/JB088iS01p0B377>.
- 495 Durham, W.B., Kirby, S.H., Stern, L.A., 1992. Effects of dispersed particulates on the rheology of water ice at planetary conditions. *Journal of Geophysical Research: Planets* 97, 20883–20897. URL: <http://dx.doi.org/10.1029/92JE02326>, doi:<https://doi.org/10.1029/92JE02326>.
- Duval, P., Ashby, M.F., Anderman, I., 1983. Rate-controlling processes in the creep of polycrystalline ice. *The Journal of Physical Chemistry* 87, 4066–4074.
- 500 Duval, P., Montagnat, M., Grennerat, F., Weiss, J., Meyssonier, J., Philip, A., 2010. Creep and plasticity of glacier ice: a material science perspective. *Journal of Glaciology* 56, 1059–1068.



- Fan, S., Cross, A.J., Prior, D.J., Goldsby, D.L., Hager, T.F., Negrini, M., Qi, C., 2021. Crystallographic preferred orientation (cpo) development governs strain weakening in ice: Insights from high-temperature deformation experiments. *Journal of Geophysical Research: Solid Earth* 126, e2021JB023173.
- 505 Fan, S., Hager, T.F., Prior, D.J., Cross, A.J., Goldsby, D.L., Qi, C., Negrini, M., Wheeler, J., 2020. Temperature and strain controls on ice deformation mechanisms: insights from the microstructures of samples deformed to progressively higher strains at -10 , -20 and -30°C . *The Cryosphere* 14, 3875–3905.
- Fan, S., Prior, D.J., Pooley, B., Bowman, H., Davidson, L., Wallis, D., Piazzolo, S., Qi, C., Goldsby, D.L., Hager, T.F., 2023. Grain growth of natural and synthetic ice at 0°C . *The Cryosphere* 17, 3443–3459.
- 510 Faria, S.H., Weikusat, I., Azuma, N., 2014. The microstructure of polar ice. part I: Highlights from ice core research. *Journal of Structural Geology* 61, 2–20.
- Gow, A.J., Williamson, T., 1976. Rheological implications of the internal structure and crystal fabrics of the west Antarctic ice sheet as revealed by deep core drilling at byrd station. *Geological Society of America Bulletin* 87, 1665–1677.
- Guillope, M., Poirier, J.P., 1979. Dynamic recrystallization during creep of single-crystalline halite: An experimental study. *Journal of Geophysical Research: Solid Earth* 84, 5557–5567.
- 515 Hidas, K., Tommasi, A., Mainprice, D., Chauve, T., Barou, F., Montagnat, M., 2017. Microstructural evolution during thermal annealing of ice-Ih. *Journal of Structural Geology* 99, 31–44.
- Hudleston, P.J., 1977. Progressive deformation and development of fabric across zones of shear in glacial ice, in: *Energetics of Geological Processes*. Springer, pp. 121–150.
- 520 Hudleston, P.J., 2015. Structures and fabrics in glacial ice: a review. *Journal of Structural Geology* 81, 1–27.
- Iliescu, D., Baker, I., 2008. Effects of impurities and their redistribution during recrystallization of ice crystals. *Journal of Glaciology* 54, 362–370.
- Iwahashi, Y., Furukawa, M., Horita, Z., Nemoto, M., Langdon, T.G., 1998. Microstructural characteristics of ultrafine-grained aluminum produced using equal-channel angular pressing. *Metallurgical and materials transactions A* 29, 2245–2252.
- 525 Iwahashi, Y., Horita, Z., Nemoto, M., Wang, J., Langdon, T.G., 1996. Principle of equal-channel angular pressing for the processing of ultra-fine grained materials. *Scripta materialia* 35.
- Jacka, T.H., Donoghue, S., Li, J., Budd, W.F., Anderson, R.M., 2003. Laboratory studies of the flow rates of debris-laden ice. *Annals of Glaciology* 37, 108–112.
- Jackson, M., 1999. Dynamics of the shear margin of ice stream B, west Antarctica. Ph.D. thesis. Caltech.
- 530 Jackson, M., Kamb, B., 1997. The marginal shear stress of ice stream b, west antarctica. *Journal of Glaciology* 43, 415–426.
- Jessell, M., Bons, P., Evans, L., Barr, T., Stüwe, K., 2001. Elle: the numerical simulation of metamorphic and deformation microstructures. *Computers & Geosciences* 27, 17–30.
- Jiang, Z., Prior, D.J., Wheeler, J., 2000. Albite crystallographic preferred orientation and grain misorientation distribution in a low-grade mylonite: implications for granular flow. *Journal of Structural Geology* 22, 1663–1674.
- 535 Journaux, B., Chauve, T., Montagnat, M., Tommasi, A., Barou, F., Mainprice, D., Gest, L., 2019. Recrystallization processes, microstructure and crystallographic preferred orientation evolution in polycrystalline ice during high-temperature simple shear. *The Cryosphere* 13, 1495–1511.
- Kamb, W.B., 1972. Experimental recrystallization of ice under stress, in: Heard, H.C., Borg, I.Y., Carter, N.L., Rayleigh, C.B. (Eds.), *Flow and Fracture of Rocks*. American Geophysical Union, pp. 211–242.



- 540 Karato, S.i., Jung, H., Katayama, I., Skemer, P., 2008. Geodynamic significance of seismic anisotropy of the upper mantle: new insights from laboratory studies. *Annu. Rev. Earth Planet. Sci.* 36, 59–95.
- Kawasaki, M., Horita, Z., Langdon, T.G., 2009. Microstructural evolution in high purity aluminum processed by ECAP. *Materials Science and Engineering: A* 524, 143–150.
- Kvackaj, T., Zemko, M., Kuskulic, T., Kocisko, R., Besterici, M., Dobatkin, S.V., Molnarova, M., 2007. Nanostructure formation and numerical simulation of if steel in ECAP. *High Temperature Materials and Processes* 26, 147–150.
- 545 Langdon, T.G., 2013. Twenty-five years of ultrafine-grained materials: Achieving exceptional properties through grain refinement. *Acta Materialia* 61, 7035–7059.
- Lapovok, R., Estrin, Y., Popov, M.V., Langdon, T.G., 2008. Enhanced superplasticity in a magnesium alloy processed by equal-channel angular pressing with a back-pressure. *Advanced Engineering Materials* 10, 429–433.
- 550 Law, R.D., 2014. Deformation thermometry based on quartz c-axis fabrics and recrystallization microstructures: A review. *Journal of Structural Geology* 66, 129–161.
- Li, J., Jacka, T.H., Budd, W.F., 2000. Strong single-maximum crystal fabrics developed in ice undergoing shear with unconstrained normal deformation. *Annals of Glaciology* 30, 88–92.
- Llorens, M.G., Griera, A., Bons, P.D., Lebensohn, R.A., Evans, L.A., Jansen, D., Weikusat, I., 2016. Full-field predictions of ice dynamic recrystallisation under simple shear conditions. *Earth and Planetary Science Letters* 450, 233–242.
- 555 Llorens, M.G., Griera, A., Steinbach, F., Bons, P.D., Gomez-Rivas, E., Jansen, D., Roessiger, J., Lebensohn, R.A., Weikusat, I., 2017. Dynamic recrystallization during deformation of polycrystalline ice: insights from numerical simulations. *Phil. Trans. R. Soc. A* 375, 20150346.
- Lutz, F., Eccles, J., Prior, D.J., Craw, L., Fan, S., Hulbe, C., Forbes, M., Still, H., Pyne, A., Mandeno, D., 2020. Constraining ice shelf anisotropy using shear wave splitting measurements from active-source borehole seismics. *Journal of Geophysical Research: Earth Surface* 125, e2020JF005707.
- 560 Lutz, F., Prior, D.J., Still, H., Bowman, M.H., Boucinhas, B., Craw, L., Fan, S., Kim, D., Mulvaney, R., Thomas, R.E., et al., 2022. Ultrasonic and seismic constraints on crystallographic preferred orientations of the priestley glacier shear margin, antarctica. *The Cryosphere* 16, 3313–3329.
- 565 Mainprice, D., Bachmann, F., Hielscher, R., Schaeben, H., 2015. Descriptive tools for the analysis of texture projects with large datasets using MTEX: strength, symmetry and components. *Geological Society, London, Special Publications* 409, 251–271.
- Monz, M.E., Hudleston, P.J., Prior, D.J., Michels, Z., Fan, S., Negrini, M., Langhorne, P.J., Qi, C., 2021. Full crystallographic orientation (c and a axes) of warm, coarse-grained ice in a shear-dominated setting: a case study, Storglaciären, Sweden. *The Cryosphere* 15, 303–324.
- Pathare, A.V., Paige, D.A., Turtle, E., 2005. Viscous relaxation of craters within the martian south polar layered deposits. *Icarus* 174, 396–418.
- 570 Piazzolo, S., Bons, P.D., Griera, A., Llorens, M.G., Gomez-Rivas, E., Koehn, D., Wheeler, J., Gardner, R., Godinho, J.R., Evans, L., et al., 2019. A review of numerical modelling of the dynamics of microstructural development in rocks and ice: Past, present and future. *Journal of Structural Geology* 125, 111–123.
- Poirier, J.P., 1985. *Creep of crystals: high-temperature deformation processes in metals, ceramics and minerals.* Cambridge University Press.
- 575 Prior, D.J., Lilly, K., Seidemann, M., Vaughan, M., Becroft, L., Easingwood, R., Diebold, S., Obbard, R., Daghlian, C., Baker, I., et al., 2015. Making EBSD on water ice routine. *Journal of microscopy* 259, 237–256.



- Qi, C., Goldsby, D.L., Prior, D.J., 2017. The down-stress transition from cluster to cone fabrics in experimentally deformed ice. *Earth and Planetary Science Letters* 471, 136–147.
- Qi, C., Prior, D.J., Craw, L., Fan, S., Llorens, M.G., Griera, A., Negrini, M., Bons, P.D., Goldsby, D.L., 2019. Crystallographic preferred orientations of ice deformed in direct-shear experiments at low temperatures. *The Cryosphere* 13, 351–371.
- 580 Qi, C., Stern, L.A., Pathare, A., Durham, W.B., Goldsby, D.L., 2018. Inhibition of grain boundary sliding in fine-grained ice by intergranular particles: Implications for planetary ice masses. *Geophysical Research Letters* 45, 12–757.
- Rathmann, N.M., Hvidberg, C.S., Grinsted, A., Lilien, D.A., Dahl-Jensen, D., 2021. Effect of an orientation-dependent non-linear grain fluidity on bulk directional enhancement factors. *Journal of Glaciology* 67, 569–575.
- 585 Richards, D.H., Pegler, S.S., Piazzolo, S., Harlen, O.G., 2021. The evolution of ice fabrics: A continuum modelling approach validated against laboratory experiments. *Earth and Planetary Science Letters* 556, 116718.
- Saruya, T., Nakajima, K., Takata, M., Homma, T., Azuma, N., Goto-Azuma, K., 2019. Effects of microparticles on deformation and microstructural evolution of fine-grained ice. *Journal of Glaciology* 65, 531–541.
- Schmid, S., Casey, M., 1986. Complete fabric analysis of some commonly observed quartz c-axis patterns. *Mineral and Rock Deformation: Laboratory Studies: The Paterson Volume* , 263–286.
- 590 Schoof, C., Hewitt, I., 2013. Ice-sheet dynamics. *Annual Review of Fluid Mechanics* 45, 217–239.
- Segal, V., 2020. Equal-channel angular extrusion (ECAE): from a laboratory curiosity to an industrial technology. *Metals* 10, 244.
- Segal, V.M., Reznikov, V.I., Drobyshevski, A.E., Kopylov, V., 1981. Plastic working of metals by simple shear. *Russian Metallurgy* 1, 99–105.
- 595 Showman, A.P., Han, L., 2005. Effects of plasticity on convection in an ice shell: Implications for Europa. *Icarus* 177, 425–437.
- Skemer, P., Katayama, I., Jiang, Z., Karato, S.i., 2005. The misorientation index: Development of a new method for calculating the strength of lattice-preferred orientation. *Tectonophysics* 411, 157–167.
- Song, M., Baker, I., Cole, D.M., 2005. The effect of particles on dynamic recrystallization and fabric development of granular ice during creep. *Journal of Glaciology* 51, 377–382.
- 600 Stern, L.A., Durham, W.B., Kirby, S.H., 1997. Grain-size-induced weakening of H₂O ices I and II and associated anisotropic recrystallization. *Journal of Geophysical Research: Solid Earth* 102, 5313–5325. URL: <http://dx.doi.org/10.1029/96JB03894>, doi:<https://doi.org/10.1029/96JB03894>.
- Thomas, R.E., Negrini, M., Prior, D.J., Mulvaney, R., Still, H., Bowman, M.H., Craw, L., Fan, S., Hubbard, B., Hulbe, C., et al., 2021. Microstructure and crystallographic preferred orientations of an azimuthally oriented ice core from a lateral shear margin: Priestley Glacier, Antarctica. *Frontiers in Earth Science* 9, 702213.
- 605 Urai, J.L., Means, W.D., Lister, G.S., 1986. Dynamic recrystallization of minerals. *Mineral and Rock Deformation: Laboratory Studies: The Paterson Volume* , 161–199.
- Valiev, R.Z., Langdon, T.G., 2006. Principles of equal-channel angular pressing as a processing tool for grain refinement. *Progress in materials science* 51, 881–981.
- 610 Vaughan, M.J., Prior, D.J., Jefferd, M., Brantut, N., Mitchell, T.M., Seidemann, M., 2017. Insights into anisotropy development and weakening of ice from in situ p wave velocity monitoring during laboratory creep. *Journal of Geophysical Research: Solid Earth* 122, 7076–7089. URL: <http://dx.doi.org/10.1002/2017JB013964>, doi:<https://doi.org/10.1002/2017JB013964>.
- Wei, W., Zhang, W., Wei, K.X., Zhong, Y., Cheng, G., Hu, J., 2009. Finite element analysis of deformation behavior in continuous ECAP process. *Materials Science and Engineering: A* 516, 111–118.



- 615 Wilson, C.J., Hunter, N.J., Luzin, V., Peternell, M., Piazzolo, S., 2019. The influence of strain rate and presence of dispersed second phases on the deformation behaviour of polycrystalline d2o ice. *Journal of Glaciology* 65, 101–122.
- Wilson, C.J.L., 1982. Texture and grain growth during the annealing of ice. *Textures and Microstructures* 5, 19–31.
- Wilson, C.J.L., Peternell, M., 2012. Ice deformed in compression and simple shear: control of temperature and initial fabric. *Journal of Glaciology* 58, 11–22.
- 620 Xia, K., Wang, J.T., Wu, X., Chen, G., Gurvan, M., 2005. Equal channel angular pressing of magnesium alloy az31. *Materials Science and Engineering: A* 410, 324–327.
- Zhao, Y.H., Liao, X.Z., Jin, Z., Valiev, R.Z., Zhu, Y.T., 2004. Microstructures and mechanical properties of ultrafine grained 7075 Al alloy processed by ECAP and their evolutions during annealing. *Acta Materialia* 52, 4589–4599.



Table 1. Summary of experiments

Sample	Graphite fraction	Passes	Load (kg)	Length (mm)	ε'	Part for analysis	φ
ECAP_33	2.1 wt.% (0.9 vol.%)	1	42.5	110	0.6	ECAP_33_1P	50°
ECAP_19	3.6 wt.% (1.5 vol.%)	1	42.5	98	0.6	ECAP_19_2P	55°
		2	37.5	100*	1.2		
		3	37.5	50	1.8	ECAP_19_3P	50°
ECAP_21	1.8 wt.% (0.8 vol.%)	1	42.5	110	0.6	ECAP_21_4P	45°
		2	37.5	105	1.2		
		3	37.5	93	1.8		
		4	32.5	85	2.4		
ECAP_34	2.6 wt.% (1.1 vol.%)	1	42.5	107	0.6	ECAP_34_5P	60°
		2	32.5	99	1.2		
		3	32.5	95	1.8		
		4	32.5	85	2.4		
		5	32.5	65	3.0		
ECAP_38	2.2 wt.% (0.9 vol.%)	1	42.5	105	0.6	ECAP_38_6P	55°
		2	32.5	100	1.2		
		3	32.5	95	1.8		
		4	32.5	95	2.4		
		5	32.5	92	3.0		
		6	32.5	94	3.6		

*An extra piece was added, so that the length is longer than or similar to that of the previous pass. This also applies to sample ECAP_38.

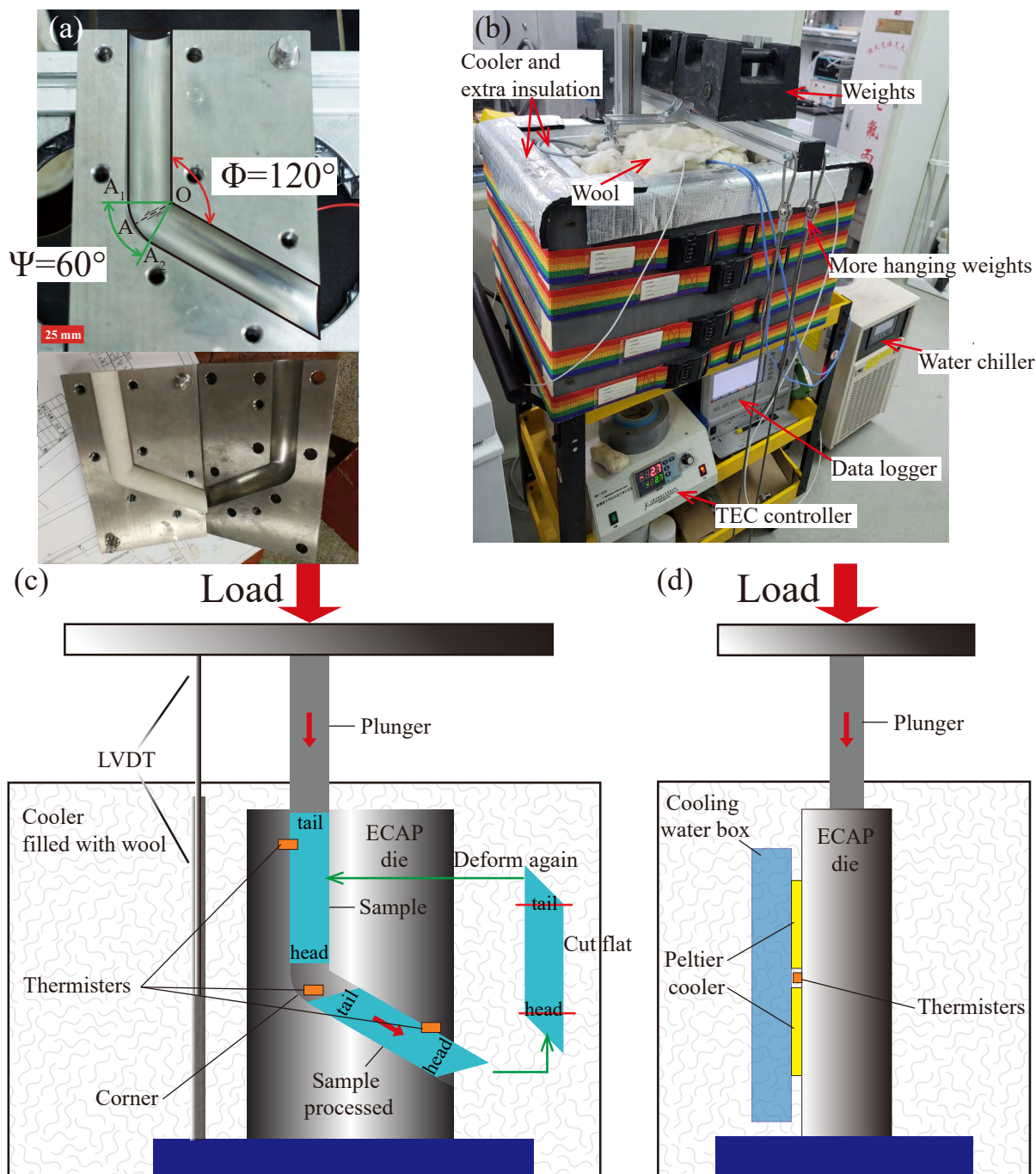


Figure 1. Photos and drawings for the ECAP apparatus. (a) Photos focusing on the channel of the ECAP die. In the top photo, the channel angle, Φ , and the curvature angle, Ψ , are illustrated. In the bottom photo, both parts of die are shown, with a dummy sample in the channel. (b) Photo of the apparatus running an experiment. (c) and (d) Drawings of the ECAP apparatus from front and side views. Thermistors are stuck to the die on the outer surface. The plunger cannot bend at the corner, such that a spare piece of ice is added to the tail of sample to push the sample through the corner. Then the spare piece is removed. All passes are done without changing the orientation of the sample.

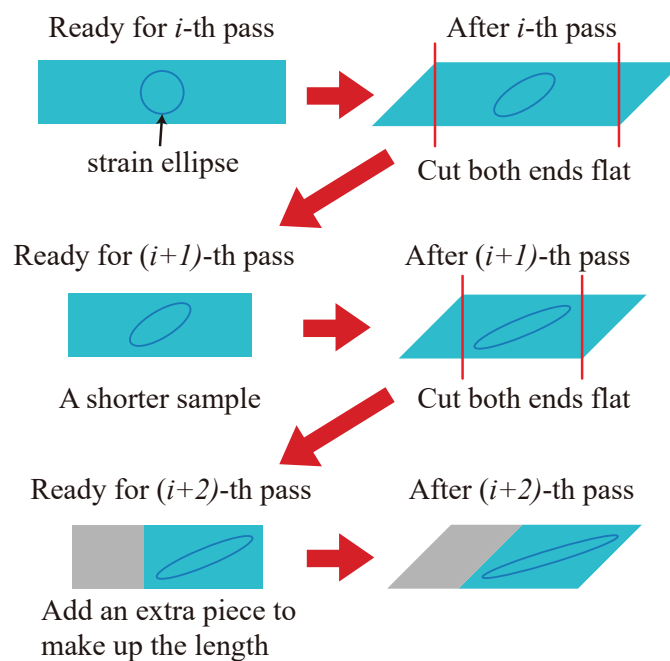


Figure 2. Drawings describing the accumulation of shear strain in a sample deformed from the i -th pass to the $(i+2)$ -th pass. For the preparation of each pass, both ends of the sample must be cut flat and perpendicular to the cylindrical axis. When the sample becomes too short, an extra piece will be added to the sample to make up the length. The circle in the sample is a strain ellipse, describing the theoretical strain accumulated by each pass.

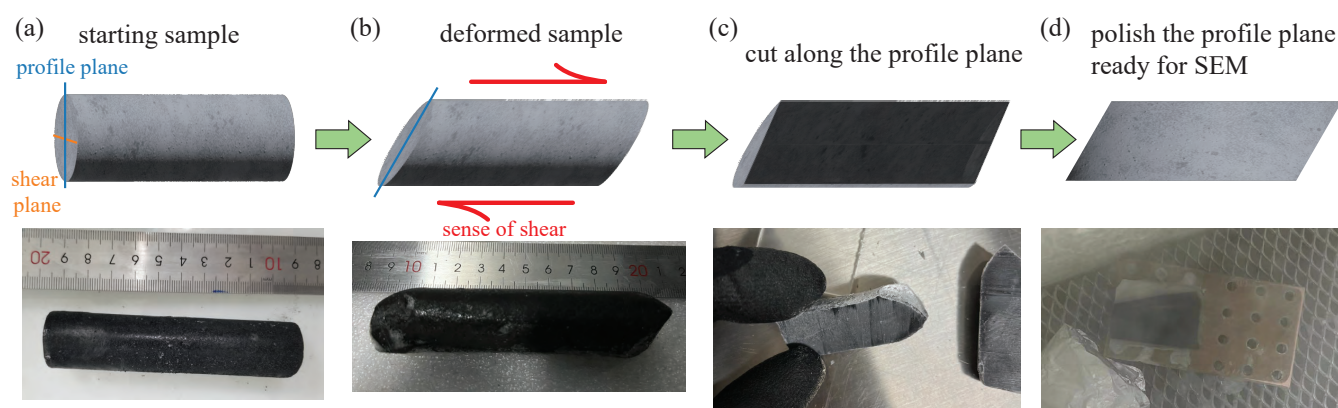


Figure 3. Illustration for a sample deformed and prepared for microstructural analysis. In each panel, a drawing is on top and a photo is at bottom. (a) Starting sample before deformation. (b) Sample deformed by ECAP. (c) Sample cut along profile plane. (d) Sample polished and mounted on a copper ingot for analysis. Note that the sample is ice + graphite, so the color is black.

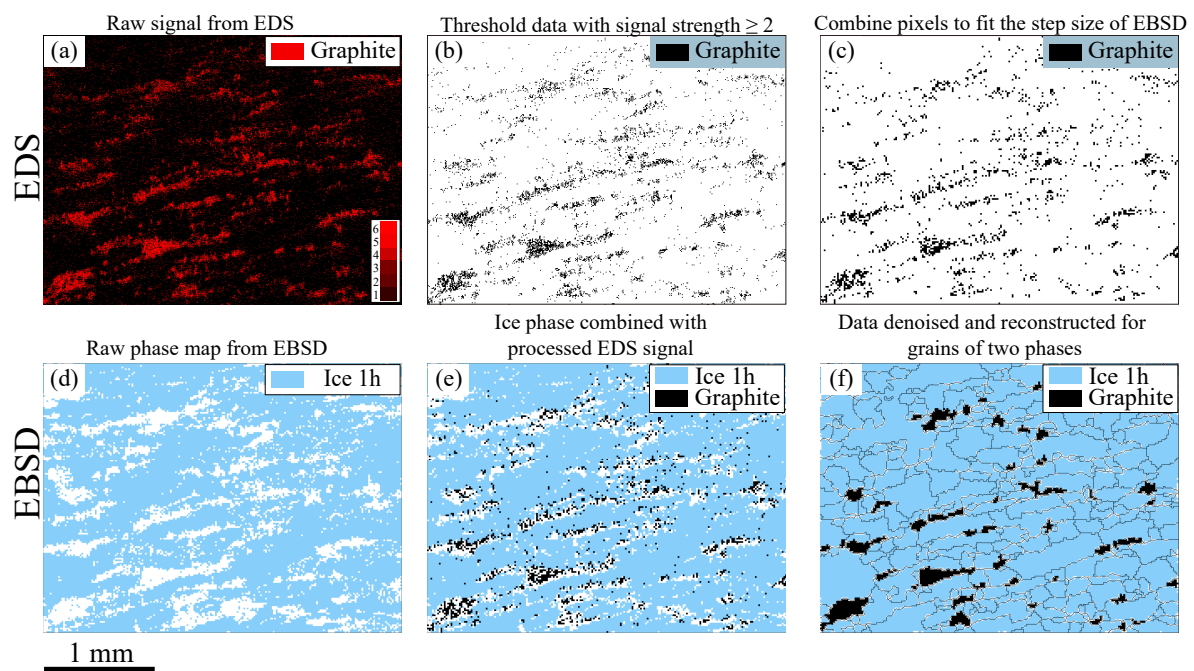


Figure 4. Illustration for the combination of EDS and EBSD data to locate the graphite phase. The example used here is sample ECAP_38_6P. (a) Raw data for carbon obtained from EDS. (b) Data with signal strength ≥ 2 . (c) Combine pixels so that the pixel size is the same as the step size of EBSD data, which is 15 μm . (d) Raw phase map processed from EBSD data. (e) Knowing the coordinates of graphite from (c), create “EBSD” data of graphite. Combine the ice phase and the graphite phase. (f) Denoise the data and reconstruct grains with MTEX toolbox. Note that by this method, the identified graphite phase represents the upper limit of the area fraction of the graphite.

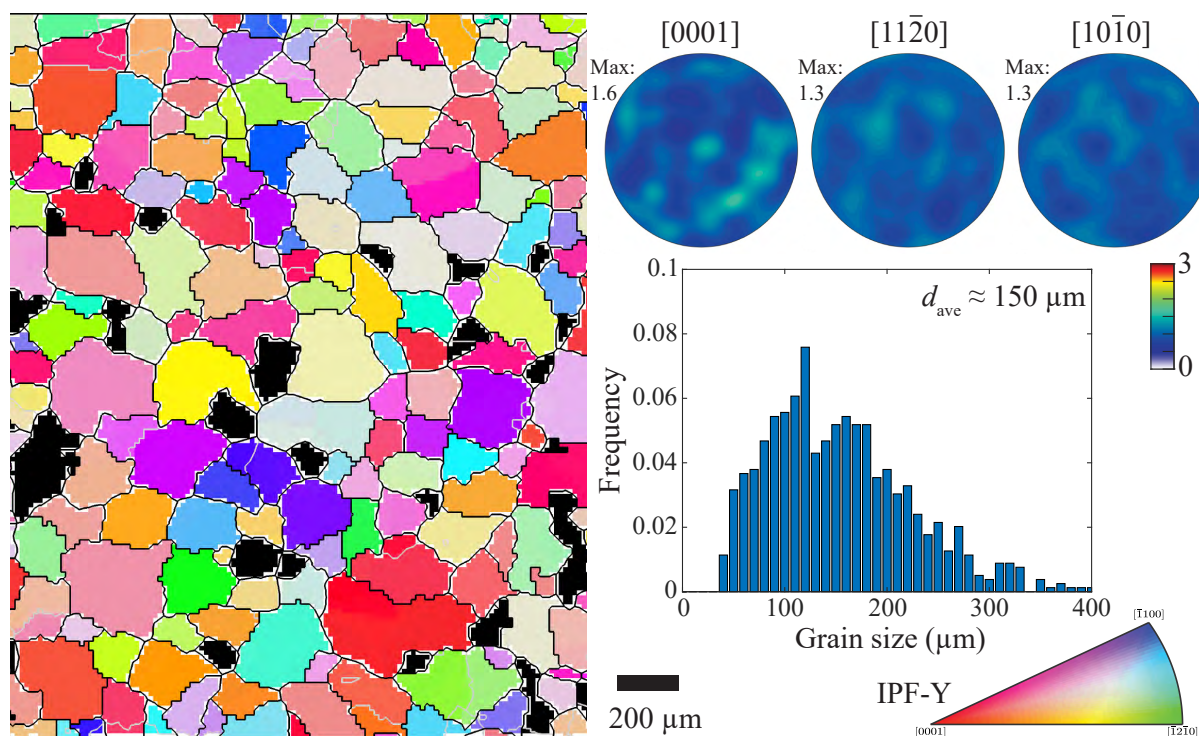


Figure 5. Microstructural analyses of an undeformed ice samples. The orientation map on the left is colored by IPF-Y, which uses the color map to indicate the specific crystallographic axis that is parallel to the y-axis. The step size is 15 μm . Grain boundaries, characterized by a misorientation of $\geq 10^\circ$, are in black, and sub-grain boundaries, characterized by a misorientation of $\geq 2^\circ$, are in gray. Graphite is in black. The stereonets on the top right are for distributions of [0001], [11 $\bar{2}$ 0] and [10 $\bar{1}$ 0] axes. Data are based on all orientation data and colored by multiples of uniform distribution (MUD), as shown in the color bar. All stereonets are equal-area lower-hemisphere projections. The histogram on the bottom-right illustrates the grain-size distribution. The grain-size data are calculated from a larger area, with 791 grains.

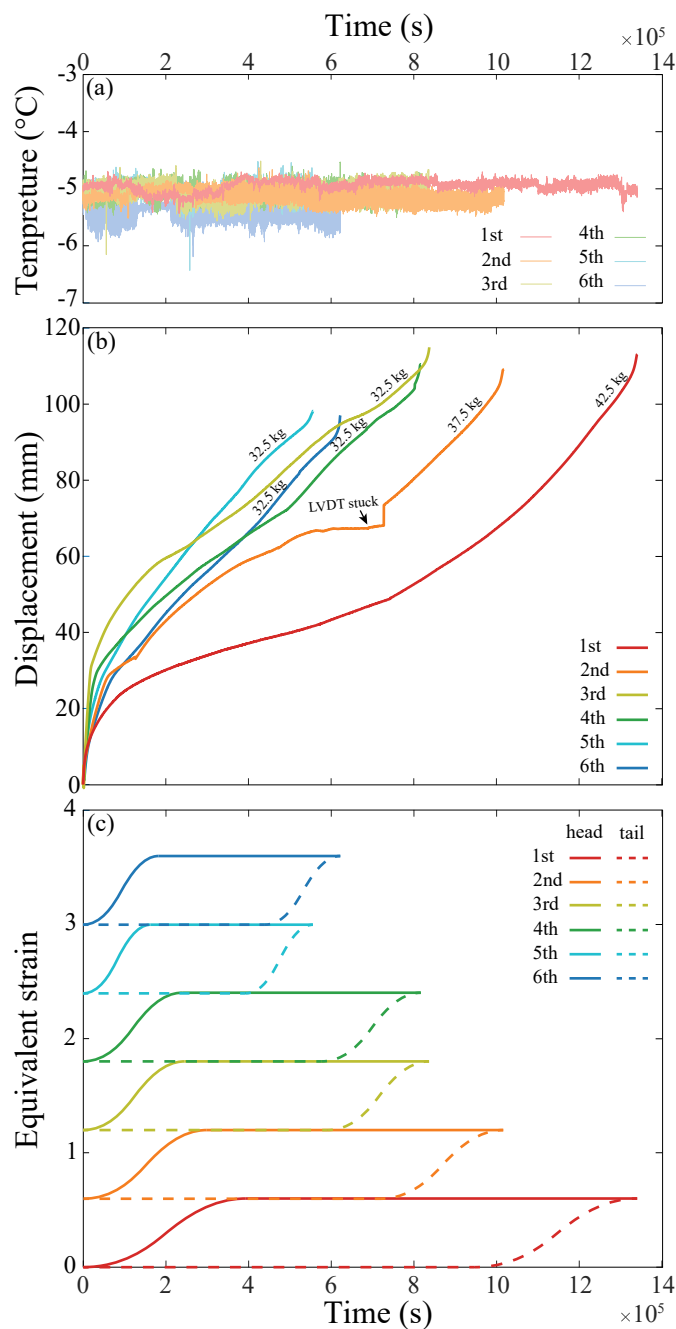


Figure 6. Plots of (a) temperature, (b) displacement and (c) nominal equivalent strain versus time for the 6 passes of sample ECAP_38. (a) The temperature is measured on the outer surface of the die, right at the corner. (b) Warmer to cooler colors mark the 1st to the 6th pass, respectively. The load for each pass is noted next to the curve. (c) Equivalent strain is estimated based on a finite element analysis of ECAP with $\Phi = 120^{\circ}$ (Wei et al., 2009).

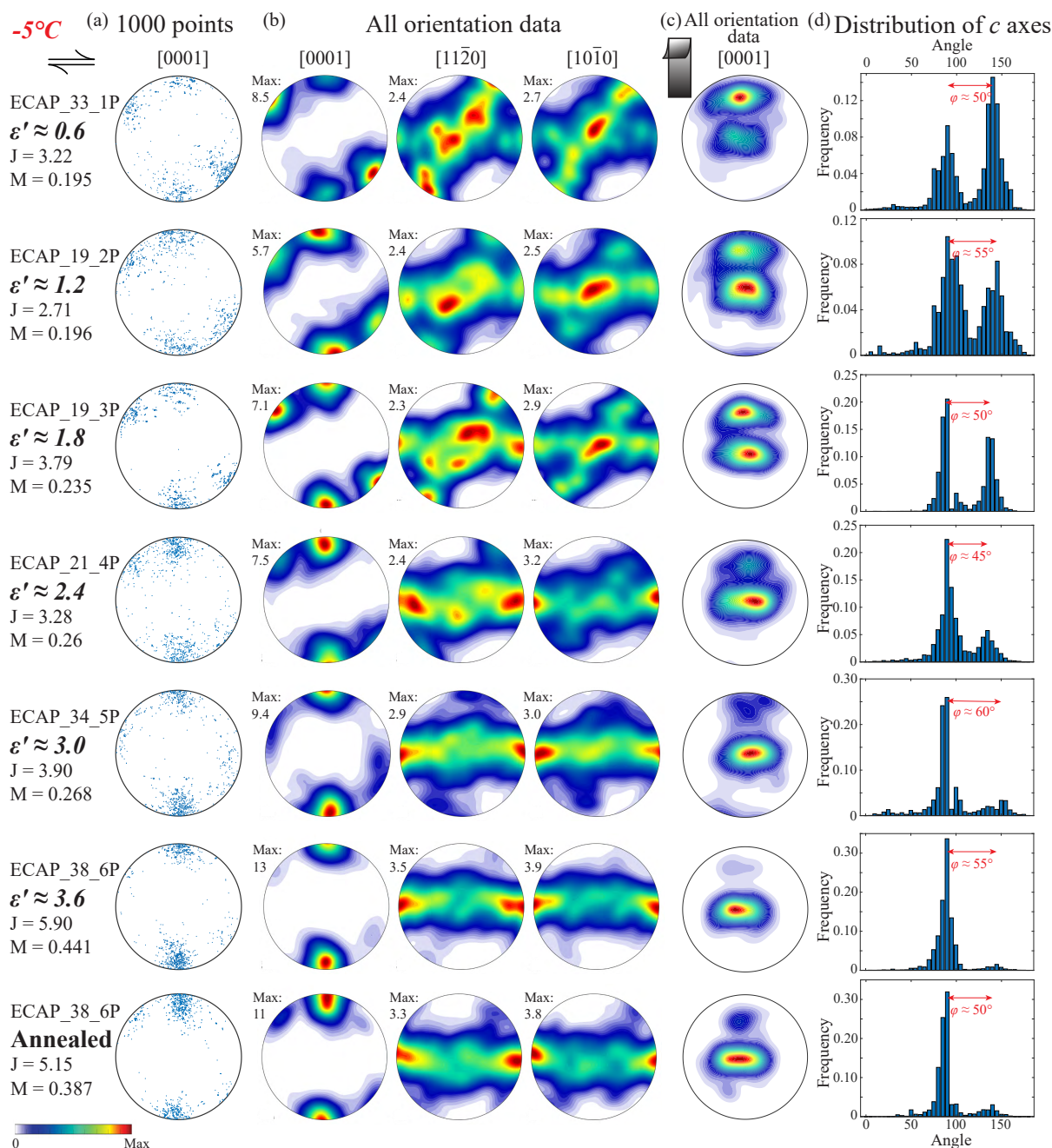


Figure 7. Analysis of crystallographic orientations on the profile plane of all deformed samples. The shear direction is top to the right, as illustrated by the black arrows. Step size is 30 μm . J and M indexes are calculated based on all orientation data. (a) Distributions of orientations of [0001] axes from 1000 randomly selected points. (b) Distributions of orientations of [0001], [11 $\bar{2}$ 0] and [10 $\bar{1}$ 0] axes contoured on the basis of all orientation data. The contours on the stereonets are colored by MUD, values of which are indicated in the color bar at the bottom of the figure. (c) Distributions of orientations of [0001] axes with the shear plane rotated to be parallel to the paper. (d) Distributions of the [0001] axes on the great circle normal to the profile plane. The angle between the two clusters, φ , is presented on each histogram. For sample ECAP_38_6p, φ is measured by taking the very weak, disappearing secondary cluster into consideration.

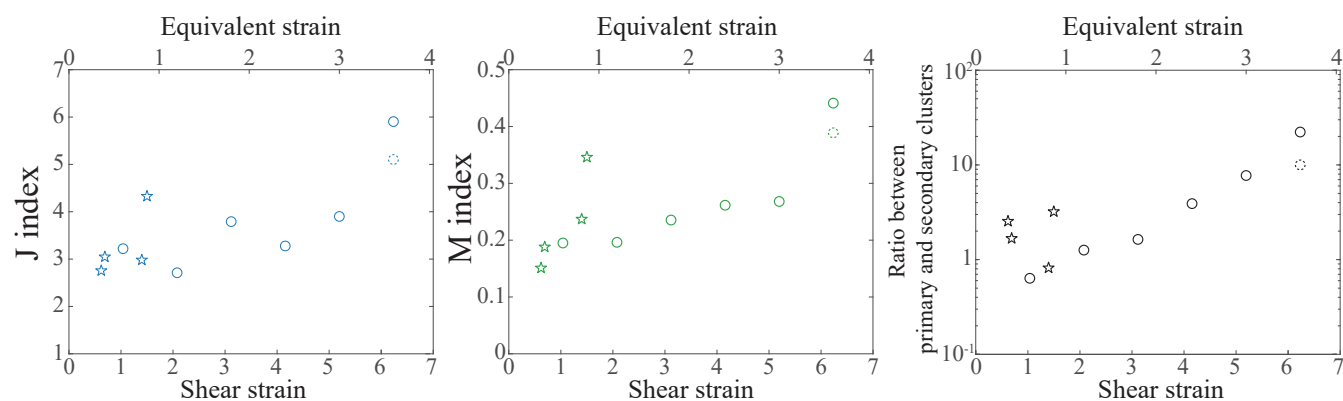


Figure 8. Crystallographic fabric strength as a function of strain. Fabric strength is quantified using (a) the J index, (b) the M index and (c) the ratio of the number of orientations in the peak of primary *c*-axis cluster over those of secondary cluster. Both values of shear strain and nominal equivalent strain are presented as x-axes. Circles are data from this study, and stars are the -5°C data from Qi et al. (2019). Circle with dashed line represents the annealed sample. The number of orientations in the peaks of the clusters are calculated from Figure 7(c).

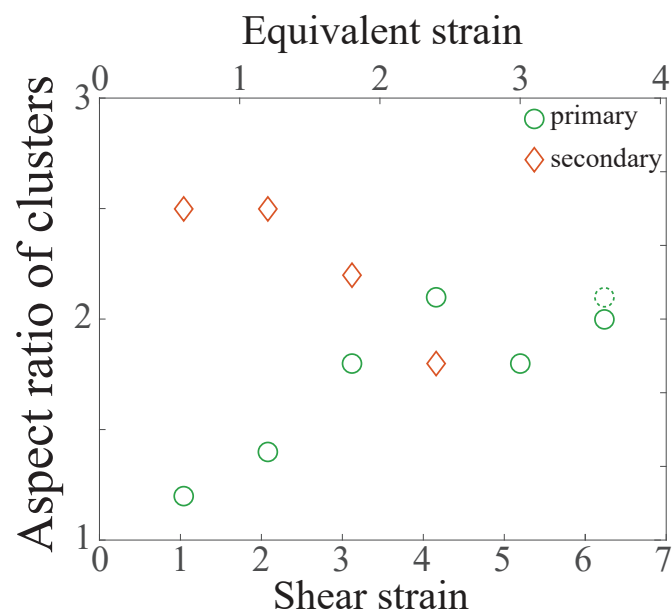


Figure 9. Aspect ratio of clusters as a function of strain. Both values of shear strain and nominal equivalent strain are presented as x-axes. Circles are for primary clusters, and diamonds are for secondary clusters. In the samples deformed to 5 and 6 passes, the secondary clusters become irregular and/or very weak, so that the aspect ratios were not calculated. The circle with dashed lines represents the annealed sample.

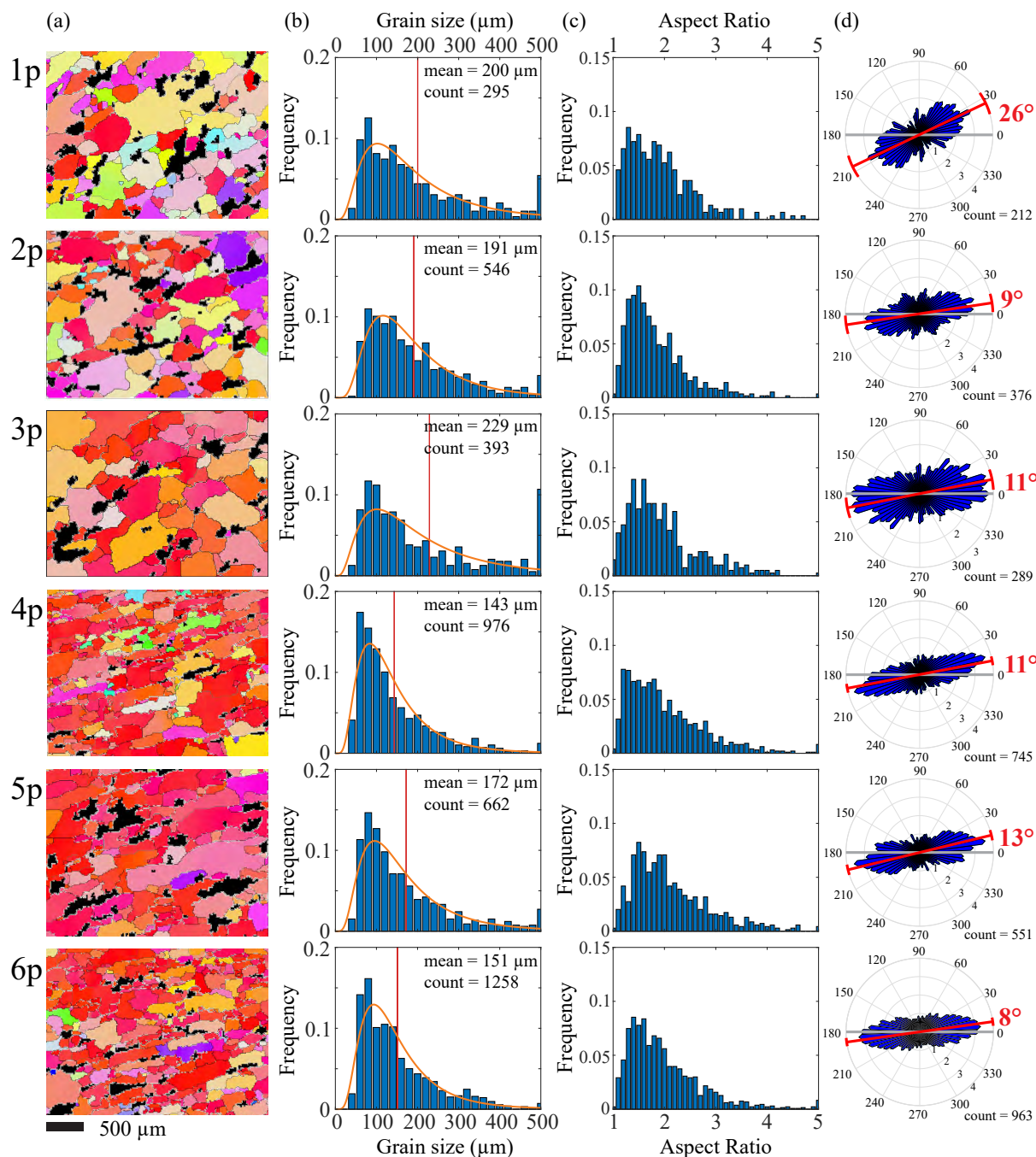


Figure 10. Microstructure results for all deformed samples. (a) Orientation maps colored by the crystallographic orientation normal to the shear plane. Graphite phase detected by EDS is black. From top to bottom are samples after 1 to 6 passes. The color map is the same as in Figure 5. In each map, grain boundaries, characterized by a misorientation of $\geq 10^\circ$, are black, and subgrain boundaries, characterized by a misorientation of $< 10^\circ$ and $\geq 2^\circ$, are gray. Unindexed spots are white. Maps are subareas of the whole mapped area. (b) Histograms for grain-size distributions. In each histogram, the red line marks the arithmetic mean, and the orange curve is a log-normal fit for the distribution. (c) Histograms for distributions of aspect ratios of grains. (d) Rose diagrams presenting shape preferred orientations. Only grains with an aspect ratio > 1.5 are counted in these diagrams.

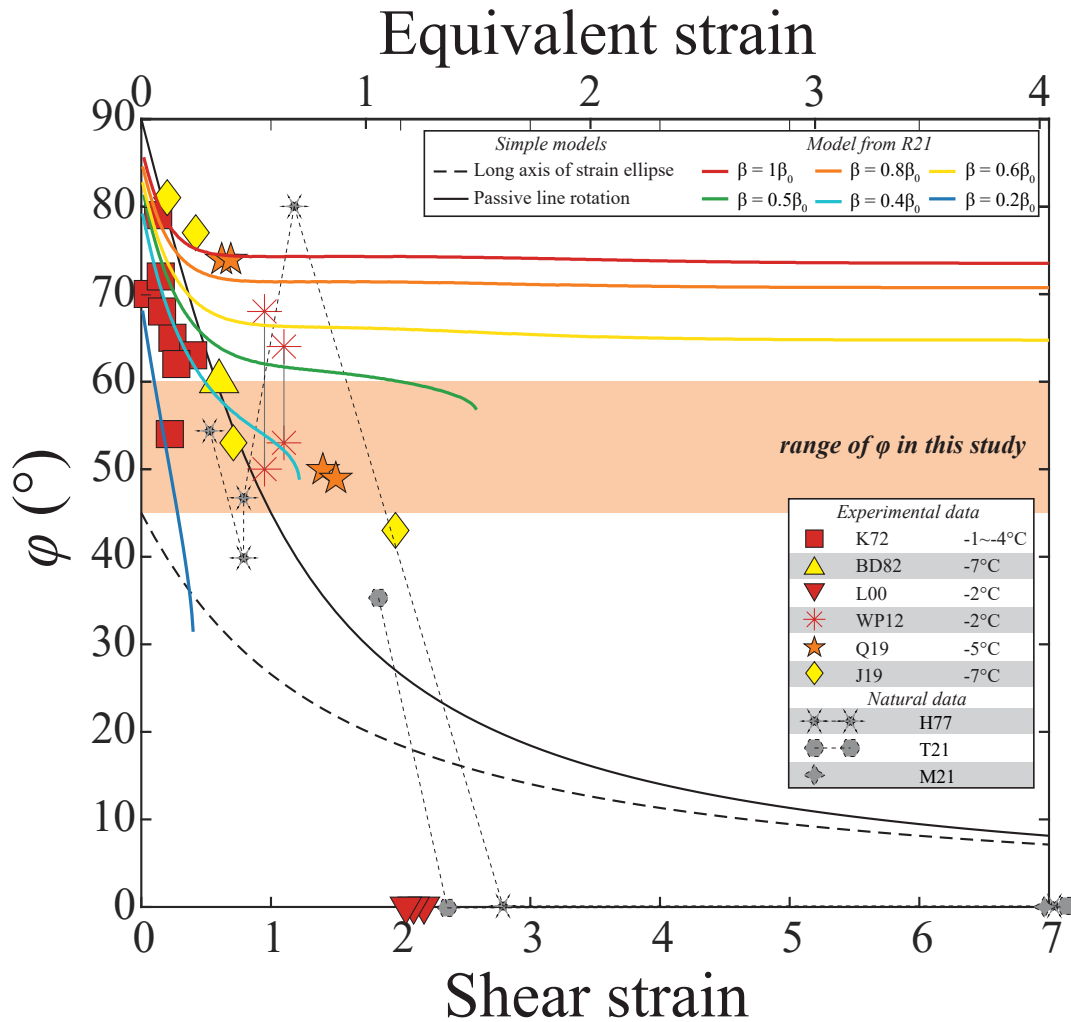


Figure 11. Plot of the angle between *c*-axis clusters, φ , for experiments from this study, experiments from the literature, results of simple models and results of numerical models. Since the nominal shear strains in this study cannot be directly compared with those in previous experimental studies, a range of φ is marked by a shaded box in the plot, independent of strain. Data point at an nominal equivalent strain of 3.6 can be treated as a single *c*-axis cluster, but a disappearing secondary cluster can still be identified, which gives a value of φ , marked by a shaded marker. Experimental data are from follows: K72: Kamb (1972); BD82: Bouchez and Duval (1982); L00: Li et al. (2000); WP12: Wilson and Peternell (2012); Q19: Qi et al. (2019); J19: Journaux et al. (2019). Only experimental data at $-5 \pm 4^\circ\text{C}$ were illustrated here. Symbol colors broadly indicate deformation temperature, with red, orange and yellow colors indicating $> -5^\circ\text{C}$, -5°C and $< -5^\circ\text{C}$, respectively. Data from natural ice are as follows: H77: Hudleston (1977); T21: Thomas et al. (2021); M21: Monz et al. (2021). Symbols tied by lines indicate they are from one sample. The maximum strains for the natural samples were estimated to be larger than the scale of our experiments, and thus, three markers (M21, H77 and T21) were placed at the right end of the x-axis suggesting that their strains are larger than 7. Outcomes from a recent published numerical model by Richards et al. (2021) are marked by colored thick lines. The parameter, β , represents the rate of migration recrystallization in the model. The termination of these curves suggests that a single-cluster fabric forms.

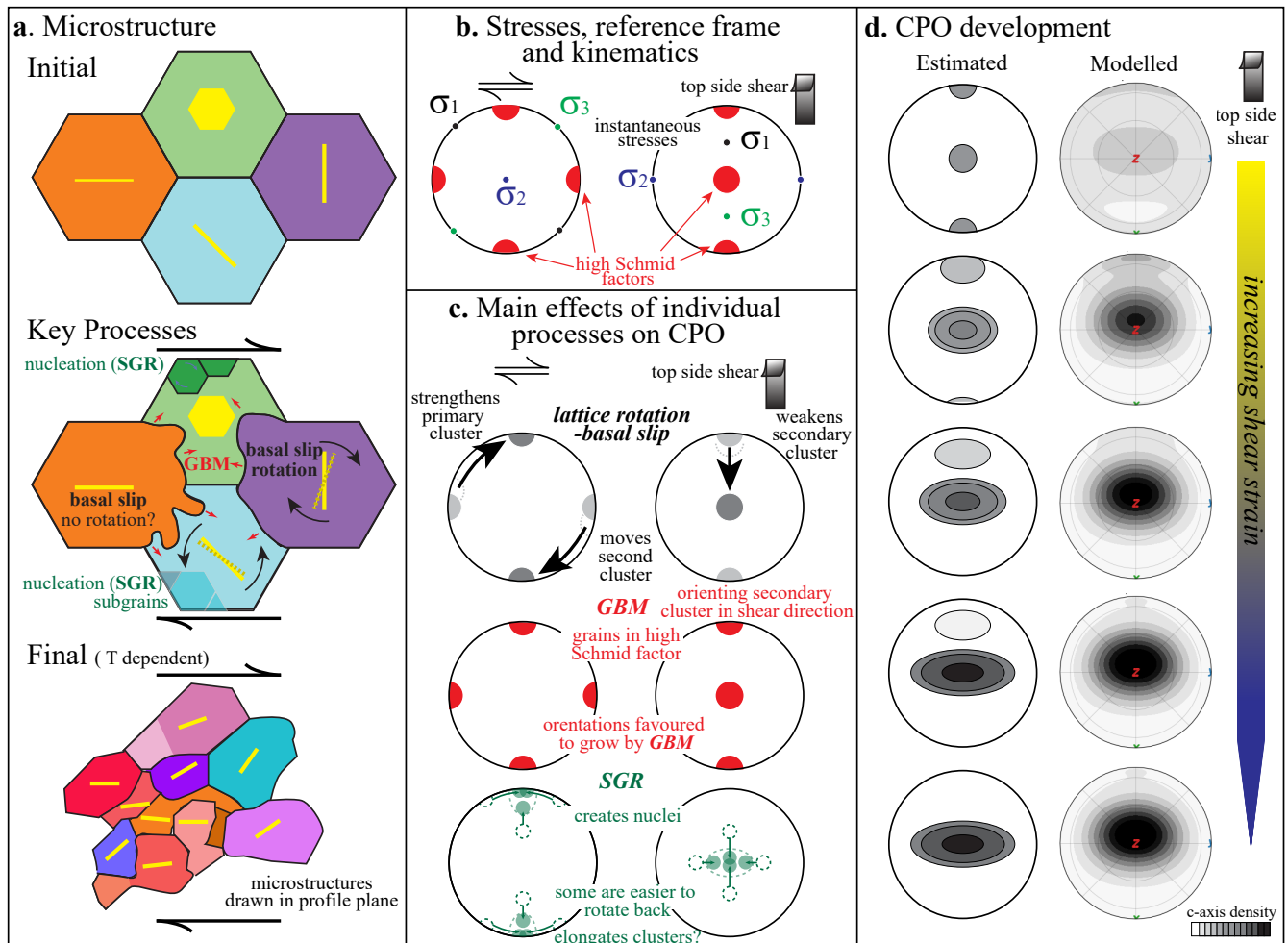


Figure 12. Schematic drawing for the development of CPOs in ice sheared in the laboratory. (a) The evolution of microstructure represented by four hexagonal grains with different initial orientation of basal planes. (b) Stress and kinematics at different reference frames. On the left, shear is top to the right; on the right, shear is to side up. Same for the next two panels. σ_1 and σ_3 are the maximum and minimum deviatoric stresses (compressive positive), respectively. (c) The main effects of CPO-formation mechanisms. In the SGR panel, longer arrows suggest faster rotation, and shorter suggest slower. (d) The development of CPOs with increasing strain. SGR: subgrain rotation. GBM: grain boundary migration.

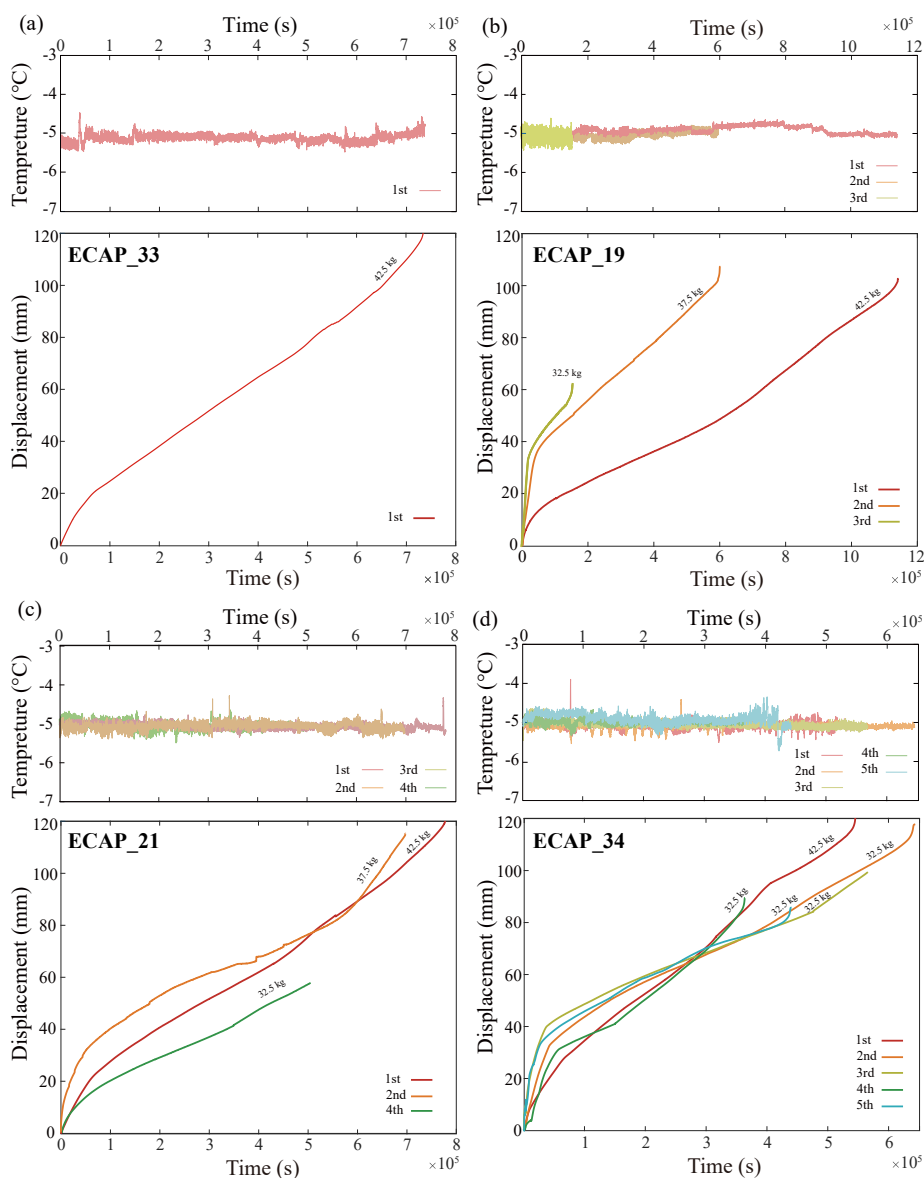


Figure A1. Plots of temperature and displacement versus time for all samples. The temperature is measured on the outer surface of the die, right at the corner. Warmer to cooler colors mark the 1st to the 5th pass, with cooler colors indicating a higher number of passes through the channels. The maximum load for each pass is noted next to the curve. (a) Sample ECAP_33. (b) Sample ECAP_19. (c) Sample ECAP_21. The temperature and displacement data of the 3rd pass were not preserved. (d) Sample ECAP_34.